Aerosol Science and Technology

ISSN: 0278-6826 (Print) 1521-7388 (Online) Journal homepage: https://www.tandfonline.com/loi/uast20

Sensitivity and accuracy of refractive index retrievals from measured extinction and absorption cross sections for mobility-selected internally mixed light absorbing aerosols

Michael I. Cotterell, Kate Szpek, Jim M. Haywood & Justin M. Langridge

To cite this article: Michael I. Cotterell, Kate Szpek, Jim M. Haywood & Justin M. Langridge (2020) Sensitivity and accuracy of refractive index retrievals from measured extinction and absorption cross sections for mobility-selected internally mixed light absorbing aerosols, Aerosol Science and Technology, 54:9, 1034-1057, DOI: 10.1080/02786826.2020.1757034

To link to this article: https://doi.org/10.1080/02786826.2020.1757034

AEROSOL SCIENCE AND TECHNOLOGY
2020, VOL. 54, NO. 9, 1034–1057
https://doi.org/10.1080/02786826.2020.1757034

Sensitivity and accuracy of refractive index retrievals from measured extinction and absorption cross sections for mobility-selected internally mixed light absorbing aerosols

Michael I. Cotterell[a,b,c], Kate Szpek[b], Jim M. Haywood[a,b], and Justin M. Langridge[a]

[a]College for Engineering, Mathematics and Physical Sciences, University of Exeter, Exeter, UK; [b]Observation Based Research, Met Office, Exeter, UK; [c]Current address: School of Chemistry, University of Bristol, Bristol, UK

ABSTRACT

Aerosol refractive index (RI) is related to particle composition and density, is used in optical spectroscopy studies to probe aerosol physiochemical properties during chemical reactions and gas-particle partitioning, and is important in atmospheric physics. Indeed, aerosol radiative forcing calculations require accurate descriptions of the real (n) and imaginary (k) RI components and their dependence on wavelength, humidity and particle mixing state. Using cavity ring-down spectroscopy (CRDS) and photoacoustic spectroscopy (PAS) to measure the extinction and absorption cross sections for mobility-selected aerosols is recognized as a good approach to retrieving n and k accurately. However, little work has assessed rigorously the sensitivity and accuracy of the retrieved values from this approach. This work investigates RI retrievals from CRDS- and PAS-measured optical properties for mobility-selected aerosols composed of ammonium sulfate (non-absorbing), nigrosin (strongly light absorbing) or a mixture of these two species. Importantly, we assess the sensitivity in our RI retrievals and then apply a Monte Carlo error propagation analysis to quantify the retrieval accuracy. Our Monte Carlo analysis is the first to account for the full range of uncertainties involved in RI retrievals from optical measurements on mobility-selected aerosol. We also report the first experimental validation of predictive RI mixing rules for non-aqueous internally mixed light absorbing aerosols by comparing mixing rule predictions with measurements for aerosol composed of internal mixtures of ammonium sulfate and nigrosin. The commonplace volume fraction mixing rule fails to predict refractive indices accurately and mixing rules with a physical basis must be used.

ARTICLE HISTORY
Received 16 January 2020
Accepted 10 April 2020

EDITOR
Hans Moosmüller

1. Introduction

Refractive index (RI, m) is an intrinsic microphysical property related to the density, molecular weight and polarizability of a substance (Liu and Daum 2008). The RI is a complex quantity with $m = n + ki$, in which n is the real component of RI describing the phase velocity of light in matter and k is the imaginary RI component characterizing light absorption. In aerosol science, accurate measurements of aerosol RI during chemical reactions (De Haan et al. 2017; Sumlin et al. 2017; Flores et al. 2014; Nakayama et al. 2013), the uptake of water in response to increases in humidity (Cotterell et al. 2017; Cai et al. 2014; Tang et al. 1997) and changes in mixing state (Cai et al. 2016; Liu and Daum 2008) allow for determination of important physiochemical parameters such as reaction rates and changes in chemical composition. Importantly, supersaturated states that are inaccessible in bulk solutions are accessed routinely in aerosols (Cai et al. 2016; Cotterell et al. 2015; Tang et al. 1997). Furthermore, reactions are often accelerated in aerosols compared to bulk solution analogs (Banerjee and Zare 2015; Lee et al. 2013, 2015), while aerosol reactions may produce entirely different products compared to those in bulk solution (Banerjee et al. 2017). These unique aerosol properties necessitate direct optical spectroscopy measurements on aerosol particles that facilitate the retrieval of aerosol RI rather than relying on bulk sample measurements.

Besides being a key microphysical property, aerosol RI is important in atmospheric optics. Provided with additional information on the aerosol shape and size

CONTACT Michael I. Cotterell, m.cotterell@bristol.ac.uk School of Chemistry, University of Bristol, Bristol, BS8 1TS, UK.
Supplemental data for this article is available online at https://doi.org/10.1080/02786826.2020.1757034

distribution, RI is used to calculate the extensive optical properties that govern aerosol-light interactions. Specifically, the extinction cross section (σ_{ext}) quantifies the fractional power removed from incident light by a particle and is the sum of the scattering (σ_{sca}) and absorption (σ_{abs}) cross sections. Quantifying the partitioning of σ_{ext} into σ_{sca} and σ_{abs} is crucial in determining whether atmospheric aerosol has a net negative or positive radiative forcing impact (Haywood and Shine 1995). Indeed, the radiative forcing impact for aerosols remains among the largest uncertainties in climate models (Alexander et al. 2013).

The calculation of cross sections from knowledge of aerosol RI and particle size describes the forward problem. Conversely, careful laboratory measurements of one or a combination of cross sections for aerosols of controlled size, shape and structure facilitate the determination of RI using inverse retrieval methods (Browne et al. 2019; Radney and Zangmeister 2018; Cotterell et al. 2016; 2017; Bluvshtein et al. 2016; Zarzana et al. 2012). Generally, these measurements involve passing an aerosol ensemble through a differential mobility analyzer that selects particles based on their electrical mobility, with mobility-selected aerosols then passed onto optical spectrometers for characterizing the extinction, scattering or absorption coefficient (α). From measurements of these attenuation coefficients in addition to aerosol number concentrations (N), the associated optical cross sections ($\sigma = \alpha/N$) are calculated. As we discuss below, studies often measure only σ_{ext} using cavity ring-down spectroscopy (CRDS), but occasionally σ_{sca} or σ_{abs} are also measured using nephelometry or photoacoustic spectroscopy (PAS), respectively. The n and k are then retrieved by comparing these measured cross sections to predictions from Mie theory.

It is commonplace in laboratory studies of aerosol optical properties to retrieve n and k from CRDS-measured σ_{ext} for mobility-selected aerosols (Toole et al. 2013; Washenfelder et al. 2013; Flores et al. 2012; Trainic et al. 2012; Zarzana et al. 2012; Hasenkopf et al. 2010; Lang-Yona et al. 2009; Dinar et al. 2008). However, Zarzana et al. (2014) show that this approach retrieves n and, to a greater extent, k with poor accuracies caused chiefly by the poor constraint on the relative fraction of σ_{ext} attributed to absorption. Therefore, recent years have seen researchers use CRDS-measured σ_{ext} in combination with PAS-measured σ_{abs} to retrieve n and k for laboratory aerosols (Radney and Zangmeister 2018; Lambe et al. 2013; Nakayama et al. 2013; Lack et al. 2006). Only few studies (e.g., the work by Khalizov et al. 2009; Xue et al. 2009) use a combined nephelometry-CRDS approach to measure σ_{sca} and σ_{ext}. The drawback of the nephelometry-CRDS measurement approach is that the light absorption fraction is often small for many aerosols of interest and the similar magnitudes of σ_{ext} and σ_{sca} provide a highly uncertain constraint on the light absorption fraction. Some studies have retrieved RI from nephelometry-measured σ_{sca} and PAS-measured σ_{abs} (Sumlin et al. 2017). However, CRDS-measured σ_{ext} values are superior in their accuracy and sensitivity compared to nephelometry-measured σ_{sca} because of the calibration-free, long path length detection inherent to the CRDS technique in addition to CRDS measuring the full impact of scattering on light extinction without requiring assumptions on truncation angles. Hence, it has become widely accepted that a good approach to laboratory studies of aerosol optical properties is to retrieve n and k from CRDS-measured σ_{ext} in combination with PAS-measured σ_{abs} (Browne et al. 2019; Radney and Zangmeister 2018; Zarzana et al. 2014). However, further uncertainties remain in other experimental parameters that continue to degrade the retrieval accuracies. Chief among these uncertainties are those in the size distribution of the mobility-selected aerosol that consists of contributions at multiple diameters arising from the quasi-Boltzmann distribution of charge on neutralized aerosol (Davies et al. 2018; Miles et al. 2010; Wiedensohler 1988). Mobility-selection of aerosol using a differential mobility analyzer (DMA) involves passing input aerosol through a neutralizer that imparts charge to aerosols before they pass through an electrostatic column that selects particles on their electrical mobility. The charge distribution imparted to aerosols in the neutralizer results in transmission of particles of different particle diameter, but the same electrical mobility, through the DMA. Therefore, RI retrieval algorithms need to account for multiple charging effects when comparing measured cross sections to Mie theory predictions.

The presence of multiply charged particles is not accounted for rigorously in many studies that instead use methods to suppress the fractional contribution of multiply charged particles to the DMA-transmitted aerosol sample (Toole et al. 2013; Zarzana et al. 2012; Hasenkopf et al. 2010; Freedman et al. 2009). Specifically, researchers configure the DMA to pass mobility diameters much larger (often >500 nm) than the median diameter of the input size distribution. At these large particle sizes, the contribution of particles containing more than one elementary charge represent <1% of the aerosol number concentration. Other studies remove multiply charged particles by passing

mobility-selected aerosol through a mass selection stage (Radney and Zangmeister 2018). Meanwhile, Khalizov et al. (2009) and Xue et al. (2009) used a tandem DMA approach that reduced, but did not eliminate, the contribution of multiply charged particles. However, the addition of secondary mass-selection or mobility-selection stages leads to a reduction in the aerosol number concentration passed to the optical spectrometers, potentially degrading the sensitivity of aerosol optical property measurements. Many studies have avoided the use of size selection methods and instead passed the full particle size distribution from the generated aerosol to CRDS and PAS instruments and the total particle size distribution is measured using a scanning mobility particle sizer (SMPS). Indeed, Radney and Zangmeister (2018) provide a summary of the studies that use this approach. However, the authors also demonstrate that retrievals of n and k from such full-distribution measurements exhibited higher uncertainties compared to those using aerosol where the particle size range was varied controllably. Importantly, select research groups have persisted with performing RI retrievals from mobility-selected aerosol while rigorously accounting for the presence of multiply charged particles in their retrieval algorithms (Flores et al. 2012, 2014), although these studies are largely restricted to retrievals from CRDS-measured σ_{ext} only. To our knowledge, only two published studies have used combined σ_{ext} and σ_{abs} measurements (using CRDS and PAS, respectively) for mobility-selected aerosol and rigorously accounted for the presence of multiple charges. Lack et al. (2006) measured values of σ_{ext} and σ_{abs} for nigrosin aerosol at a wavelength of 532 nm, corrected these cross sections for multiple charge effects using the method of Hoppel (1978) and compared these corrected cross sections to Mie theory predictions that used literature RI values for nigrosin. The second study, by ourselves, performed similar measurements but for wavelengths of 405, 514 and 658 nm (Davies et al. 2018). We demonstrated agreement between measured and predicted cross sections at wavelengths that span the visible spectrum to within 8%. Moreover, we verified that the calibration of PAS instruments using ozone-laden gas was an accurate approach for measurements at visible wavelengths. To our knowledge, no study has assessed comprehensively the sensitivity and accuracy of n and k retrievals using combined CRDS-PAS measurements for mobility-selected aerosols with a retrieval algorithm fully accounting for the presence of multiply charged particles.

This work used both CRDS and PAS in RI retrievals for mobility-selected aerosol at wavelengths of 405 and 658 nm. We report RI retrievals for ammonium sulfate (a non-absorber) and nigrosin aerosol (a strong light absorber) and compare our retrievals to previously reported values. Our measurements allow assessments of the precision and sensitivity in our retrievals; while Zarzana et al. (2014) discussed the theoretical sensitivities of RI retrievals from extinction-only and extinction and absorption measurements, we present the first assessment of RI retrieval sensitivity and precision using measured data. Moreover, we use a Monte Carlo error propagation analysis to quantify our retrieval accuracies. We demonstrate the utility of our retrieval technique to address pertinent questions in aerosol science by comparing the n and k from predictive mixing rules with measured values for internally mixed light absorbing aerosol composed of ammonium sulfate and nigrosin. To our knowledge, this is the first study testing predictive RI mixing rules for non-aqueous internally mixed light absorbing aerosols.

2. Experimental and numerical methods

The following sections describe our experimental methods (Sections 2.1–2.3), the retrieval of n and k from measured σ_{ext} and σ_{abs} for mobility selected aerosols (Section 2.4) and the charge distribution description used in the RI retrieval (Section 2.5).

2.1. Aerosol generation and conditioning

Figure 1a summarizes the methods used to generate, condition and mobility-select aerosol. Aqueous stock solutions were prepared containing the chemical solute of interest, with a solute concentration of 3 g L^{-1} dissolved in high-purity deionized water (VWR Chemicals). The dissolved solute was composed of water-soluble nigrosin dye (Sigma Aldrich, CAS number 8005-03-6, lot number MKBR1705V), ammonium sulfate (Sigma Aldrich, CAS number 7783-20-2, purity >99.0%), or a controlled mixture of both solutes. The stock solution passed to the input of a constant output atomizer (TSI 3076). A constant flow of high purity (99.999%) zero air from a gas cylinder with an outlet pressure of 900 hPa generated aqueous aerosol that passed through two indicating silica gel diffusion driers (TOPAS DDU-570) that dried the aerosol sample to a relative humidity of <5%, as determined by a humidity probe placed immediately after the second drier. Both nigrosin, ammonium sulfate and their

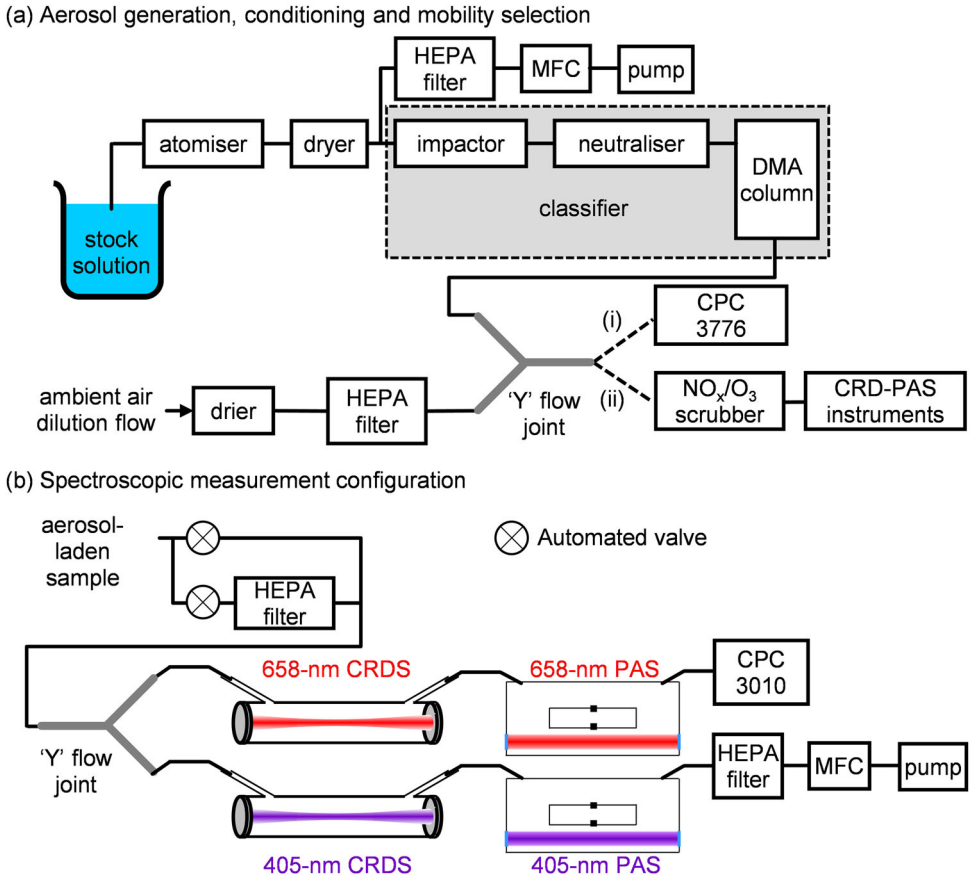

Figure 1. (a) The experimental configuration for aerosol generation, conditioning and mobility-selection prior to measurements of either the pre-DMA aerosol sample size distribution using a scanning mobility particle sizer configuration by passing the sample to a CPC_{3776}, or aerosol optical properties by passing the aerosol to our CRDS-PAS instruments. (b) The configuration used for spectroscopic measurements of aerosol extinction and absorption coefficients using CRDS and PAS, respectively. A CPC_{3010} sampled aerosol from the exit port of the 658-nm PAS for measurements of aerosol number concentration.

internal mixtures are known to equilibrate rapidly with the surrounding relative humidity (for example, see the growth factor measurements by Langridge et al. (2013) that use a similar drying method). Therefore, the aerosols after the diffusion driers are expected to be completely dry. The dried aerosol sample passed to a particle electrostatic classifier (TSI 3082) via an inertial impactor with an orifice diameter of 457 µm. The aerosol sample was charged using a soft x-ray neutralizer (TSI 3088) before passing to a DMA (TSI 3081). The DMA was operated with a negative polarity and the sheath flow rate was set to 3.5 L min^{-1}. The aerosol sample flow through the DMA was checked using a flow meter (Alicat Whisper). The sample flow rate was controlled to a value in the range 0.32 – 0.36 L min^{-1}, i.e. to a value that maintained a 1:10 aerosol-to-sheath flow rate ratio as recommended by the manufacturer, by drawing a fraction of the pre-impactor sample through a HEPA filter and mass flow controller (Alicat) to an exhaust. The mass flow rate on this mass flow controller was set at values in the range 0.00 - 0.32 standard L min^{-1}.

The desired mobility diameter for singly charged particles was set on the classifier, with the applied voltage to the DMA electrode determined by a recent manufacturer calibration. The DMA transmitted positively charged aerosols with the desired electrical mobility. In measurements reported here, we chose several values of mobility-selected diameter over the range 120–340 nm. This particle diameter range was chosen based on the theoretical work of Zarzana et al. (2014) that demonstrated n and k retrievals for both absorbing and non-absorbing aerosols are most sensitive over this range. The mobility-selected aerosol passed to one input of a 'Y' flow splitter in the configuration shown in Figure 1a. Dried and HEPA-filtered laboratory air was drawn through the other input of the 'Y' splitter to dilute the aerosol sample. The dilution flow rate was determined by the difference in flow rates between that demanded at the output of the 'Y' splitter (i.e., the flow rate required by either a

condensation particle counter or our CRDS-PAS instruments) and the aerosol flow rate input to the splitter from the DMA. The diluted aerosol sample passed to either (i) a condensation particle counter (CPC_{3776}, TSI 3776) in a scanning mobility particle sizer (SMPS) configuration, or (ii) the CRDS-PAS instruments for measurement of the aerosol optical properties. The SMPS provided important information on the pre-DMA aerosol size distribution that is needed in later calculations (see Section 2.4) of the aerosol size distribution exiting the DMA; without an additional classifier (using a tandem DMA approach), it was not possible to measure directly the output size distribution from our DMA and therefore we used the pre-DMA aerosol size distribution in combination with the classifier transfer function to calculate the transmitted aerosol size distribution. In SMPS measurements, the CPC_{3776} sampled using a flow rate of 0.3 L min^{-1} and the SMPS scans provided measurements of the multiple charge and diffusion corrected size distribution over the particle mobility diameter range 12.6 – 763.5 nm. When the sample output from the 'Y' splitter passed to our CRDS-PAS instruments, the sample first passed through an activated carbon honeycomb scrubber (Mast Carbon) to remove trace gas species such as NO_x and O_3 that can contribute to light absorption.

2.2. Measurements of extinction and absorption cross section

The CRDS and PAS instruments used in this work are contained within a single state-of-the-art instrument designed to operate in both the laboratory (Cotterell et al. 2019a; Davies et al. 2018) and aboard the FAAM BAe-146 research aircraft for characterizing atmospheric aerosol (Peers, Francis, Abel, et al. 2019, Peers, Francis, Fox, et al. 2019; Szpek et al. 2020; Davies et al. 2019). We have described this instrument thoroughly in previous work, with the instrument consisting of four CRDS and five PAS spectrometers operating at wavelengths of 405, 514 and 658 nm. We only used a selection of these spectrometers in measurements for this work, with Figure 1b showing an overview schematic of the spectroscopy configuration used here. We have described the construction, operation and performance of our CRDS and PAS instruments in previous work (Cotterell et al. 2019a; Davies et al. 2018); for completeness, we have included complete descriptions of our CRDS and PAS measurements and associated data processing for determination of aerosol extinction and absorption coefficient in Section S1 and S2 of the online supplementary information (SI). Importantly, we used two different PAS cell geometries. The 658-nm PAS used the cell geometry reported by Lack et al. (2006) that has since been adopted by numerous research groups (Foster et al. 2019; Davies et al. 2018; Fischer and Smith 2018; Bluvshtein et al. 2017). Meanwhile, the 405-nm PAS used an optimized cell geometry that we reported recently (Cotterell et al. 2019c) and that was designed using a finite element method modeling framework (Cotterell et al. 2019b) to simulate the acoustic responses for a range of photoacoustic cells. After the common sample inlet to the CRDS-PAS instrument, two automated valves controlled whether the aerosol-laden sample passed through or bypassed a HEPA filter. The automated control of passing filtered sample through our spectrometers provided regular background measurements needed for baseline values of cavity ring-down time and photoacoustic response (see Section S1 and S2) in the absence of any light extinguishing aerosol. The sample then passed to a 'Y' splitter (Brechtel) that distributed the sample flow to two CRDS instruments operating at wavelengths of 405 and 658 nm. After each CRDS instrument, the sample passed in a serial flow configuration to a photoacoustic spectrometer operating at the same wavelength. The sample flow through the 405-nm spectrometers was controlled by a mass flow controller (Alicat MC Series) located after the 405-nm PAS and was set at 1 L min^{-1}. A condensation particle counter (CPC_{3010}, TSI 3010) operating with a flow rate of 0.96 L min^{-1} controlled the sample flow through the 658-nm spectrometers. The CPC_{3010} measured the particle number concentration that was used in calculations of cross sections from the spectroscopy-measured attenuation coefficients.

2.3. Aerosol number concentration measurements

To measure σ_{ext} and σ_{abs} at each mobility-selected diameter, the measured extinction and absorption coefficients were divided by the corresponding aerosol number concentration for each spectrometer. The aerosol number concentration in each spectrometer was determined using measured number concentrations from the CPC_{3010} located immediately after the 658-nm PAS instrument in combination with characterized aerosol transmission coefficients for each spectrometer. Section S3 of the SI describes how we calibrated the CPC_{3010}, while Section S4 describes how the measurement of number concentration at the exhaust of the 658-nm PAS was corrected to account

for differences in aerosol transmission through each spectrometer.

2.4. Refractive index retrievals from cross sections for mobility-selected aerosol

Mobility-selected aerosols were passed to our CRDS and PAS spectrometers. For each measurement *data set*, 12 values of mobility-selected diameter (D_{select}) were used over the range 120–340 nm in 20 nm intervals. For each D_{select}, the extinction and absorption coefficients and particle number concentration were recorded at 1 Hz sampling frequencies for five minutes. From these measurements, the aerosol number concentrations in each spectrometer were calculated using the methods described in Section 2.3, and σ_{ext} and σ_{abs} were calculated. The mean values and associated standard deviations for σ_{ext} and σ_{abs} were calculated for each five minute period corresponding to a mobility-selected diameter. The variation in the mean cross sections with D_{select} were then compared with predicted cross sections for trial values of RI and, by performing this comparison for a range of trial refractive indices, the best fit values for n and k were found. We now describe the model used to predict cross sections for a given value of D_{select} before describing how the measured and predicted cross sections were compared for the retrieval of n and k.

The output size distribution from the DMA depends on the input particle size distribution, the aerosol charge distribution, and the transfer function for the DMA. The transfer function describes the probability that a particle of a given diameter is transmitted through the DMA. Our previous publication describes how we calculated the DMA transfer function (Davies et al. 2018). Briefly, we used the equations of Stolzenburg (1988) to calculate the transfer function that included the effects of diffusion broadening. These equations require input values of D_{select}, the DMA geometry (length and radii of inner and outer electrodes), and the sheath and aerosol flow rates. This diffusion-corrected transfer function consists of multiple transmission peaks that arise from particles containing multiple units n_e of elementary charge but with similar electrical mobility. We calculated the transfer function for particles with up to six units of positive elementary charge; we remind the reader that our experiments used a negative DMA electrode polarity that results in the transmission of positively charged aerosol. We then multiplied this transfer function by the probability distribution that a particle of a given diameter contains n_e charges. This charging probability distribution depends on the performance and type of neutralizer used (Tigges et al. 2015a). Our previous work used the Wiedensohler (1988) parameterization for a radioactive neutralizer. However, as discussed in Section 2.5, this work uses an optimized charge distribution based on the Gunn equation (Gunn 1955); this approach was motivated by the fact we used a soft X-ray neutralizer in our measurements. Figure S2a in the SI shows an example transfer function calculated for $D_{select} = 200$ nm using typical values for sheath and aerosol flow rate, including corrections for both diffusion broadening and the charging probability distribution.

To model the aerosol size distribution transmitted through the classifier, we multiplied the diffusion- and charge-corrected transfer function by the aerosol size distribution input to the classifier. To characterize this latter size distribution, we operated the classifier as part of an SMPS (see Section 2.1). Four SMPS-measured size distributions were recorded for both before and after CRDS-PAS measurements of mobility-selected aerosols, with eight SMPS-measured size distributions recorded in total. We have previously shown that the SMPS-measured size distributions were stable over the data set measurement period for nigrosin (Davies et al. 2018), while we find similar stabilities in the measured size distribution for the measurements performed for this work, although the inertial impactor prior to the classifier required cleaning more regularly (every 15 min) for ammonium sulfate aerosol. We therefore calculated the mean aerosol size distribution for the data set by averaging over the eight measured size distributions. We multiplied this mean size distribution by the diffusion- and charge-corrected transfer function, and normalized the subsequent distribution such that the total number concentration is equal to one. Figure S2b (in the SI) shows an example of the normalized model size distribution transmitted through the DMA (denoted $N_N(D)$) for $D_{select} = 200$ nm, demonstrating the low contribution of $n_e > 2$ particles to the total number concentration.

To calculate the predicted values for extinction and absorption cross section, we weight $N_N(D)$ by the associated Mie cross section at each diameter. Previous studies have shown that the morphologies of aerosols composed of ammonium sulfate (AS), nigrosin or mixtures of both species are well approximated by spherical particles (Radney and Zangmeister 2018; Lack et al. 2006). Therefore, Mie theory is appropriate for optical property calculations for the aerosols of interest here. Figure S2c,e in the SI shows the particle size dependence in the Mie σ_{ext} at optical wavelengths

of 405 and 658 nm, respectively, for AS aerosol. Meanwhile, Figure S2d,f in the SI shows the fractional extinction contribution at each diameter to the ensemble-averaged extinction cross section for D_{select} = 200 nm. This latter figure shows clearly the large contribution of high-n_e particles to the ensemble-mean extinction, with n_e = 1, 2, 3, 4, 5 and 6 particles contributing 17.7%, 37.5%, 27.2%, 10.9%, 5.4% and 1%, respectively, to the total ensemble extinction in this illustrative example. Thus, it is important to account fully for highly charged particle contributions to cross sections rather than applying simple corrections that account for the presence of the n_e = 2, 3 particles only that dominate the number particle distribution. Therefore, to calculate the ensemble-average cross sections used in comparisons against measurements, we evaluate the sum:

$$\sigma_{\text{model}} = \sum_i \sigma_i(D_i) N_N(D_i) \tag{1}$$

in which the summation is performed over each diameter D_i in the model size distribution, σ_i is the Mie cross section, and σ_{model} denotes the ensemble-average cross section. The RI was retrieved by comparing the measured σ_{ext} and σ_{abs} for mobility-selected data sets with predicted values, trialing a range of values for n and k in model calculations of σ_{model}. Typically, n was varied over the range 1.35–2.00 in 0.001 intervals and k over the range 0.00 to 0.40 in 0.001 intervals. In comparing measured and model cross sections, all parameter sets {n, k} were trialed. For each {n, k} parameter set, the merit function χ^2_{total} was calculated using:

$$\chi^2_{\text{total}} = \chi^2_{\text{ext}} + \chi^2_{\text{abs}} \tag{2}$$

with χ^2_{ext} defined by:

$$\chi^2_{\text{ext}} = \frac{1}{N}\sum_i \frac{\left(\sigma_{\text{ext,i}} - \sigma_{\text{model, ext, i}}\right)^2}{\epsilon^2_{\text{ext, i}}} \tag{3}$$

and χ^2_{abs} defined by:

$$\chi^2_{\text{abs}} = \frac{1}{N}\sum_i \frac{\left(\sigma_{\text{abs,i}} - \sigma_{\text{model, abs, i}}\right)^2}{\epsilon^2_{\text{abs, i}}} \tag{4}$$

In these equations, $\sigma_{\text{ext,i}}$ and $\sigma_{\text{abs,i}}$ are the mean measured ensemble-average extinction and absorption cross sections for a given D_{select} value, $\sigma_{\text{model,ext,i}}$ and $\sigma_{\text{model,abs,i}}$ are the corresponding predicted cross sections, $\epsilon_{\text{ext, i}}$ and $\epsilon_{\text{abs, i}}$ are the associated standard deviations in the measured cross sections, and N is the number of mobility-selected diameters used in the data set with $N = \sum i$. The best-fit RI corresponds to the values of n and k that minimize χ^2_{total}.

2.5. An optimized charge distribution for a soft x-ray neutralizer

Aerosols are charged prior to the DMA by passing through a bipolar neutralizer. The three main types of neutralizer used are radioactive sources, soft x-ray neutralizers, and electrical ionizers. Within the neutralizer, gas molecules are ionized and the charged ions diffuse to aerosol surfaces to impart charge. These positive and negative ions have ion mobilities Z_+ and Z_-, respectively, and number concentrations c_+ and c_-. Aerosols may have multiple charges, with the number of charges imparted to particles following a Boltzmann-like distribution. A rigorous treatment of aerosol charging was developed by Fuchs (1963). However, the Fuchs equations cannot be solved analytically and require solving numerically. Most models of radioactive neutralizer charge distributions use the Wiedensohler (1988) parameterization that was developed by parameterizing the numerically calculated values of Fuchs charging probabilities, with the Fuchs model taking input values of mean ion mobility measured for a radioactive neutralizer (Wiedensohler et al. 1986) and assuming $c_+ = c_-$. Recently, Tigges et al. (2015b) developed a similar parameterization for soft x-ray neutralizers. The Wiedensohler or Tigges et al. parameterisations only provide charging probabilities for aerosols with charges $q = 0, \pm 1e, \pm 2e$, in which e is the elementary charge. For higher charge states, the Gunn approximation can be used (Gunn 1955):

$$f(q) = \frac{e}{\sqrt{4\pi^2\varepsilon_0 D_p kT}} \exp\left[-\frac{\left(q - \frac{2\pi\varepsilon_0 D_p kT}{e^2}\ln\left(\frac{c_+ Z_+}{c_- Z_-}\right)\right)^2}{\frac{4\pi\varepsilon_0 D_p kT}{e^2}}\right] \tag{5}$$

in which ε_0 is the vacuum permittivity, D_p is the aerosol physical diameter, k is the Boltzmann constant and T is the absolute temperature.

Our previous work used the Wiedensohler parameterization to describe charge distributions for $q/e = 0$, ±1, ±2 and the Gunn formula to describe the charge distribution for q/e = ±3, ±4, ±5, ±6 (Davies et al. 2018). Using these descriptions of charge distribution, we achieved good agreement between measured and modeled cross sections (for both σ_{ext} and σ_{abs}) for mobility-selected aerosol charged using an electrical neutralizer. However, we used a soft x-ray neutralizer in experiments for the current work. Logically, our initial approach to modeling the aerosol charge distribution was to use the Tigges parameterization for an x-ray source to describe $q/e = 0$, ±1, ±2 and the Gunn formula for higher charge states, with the Gunn

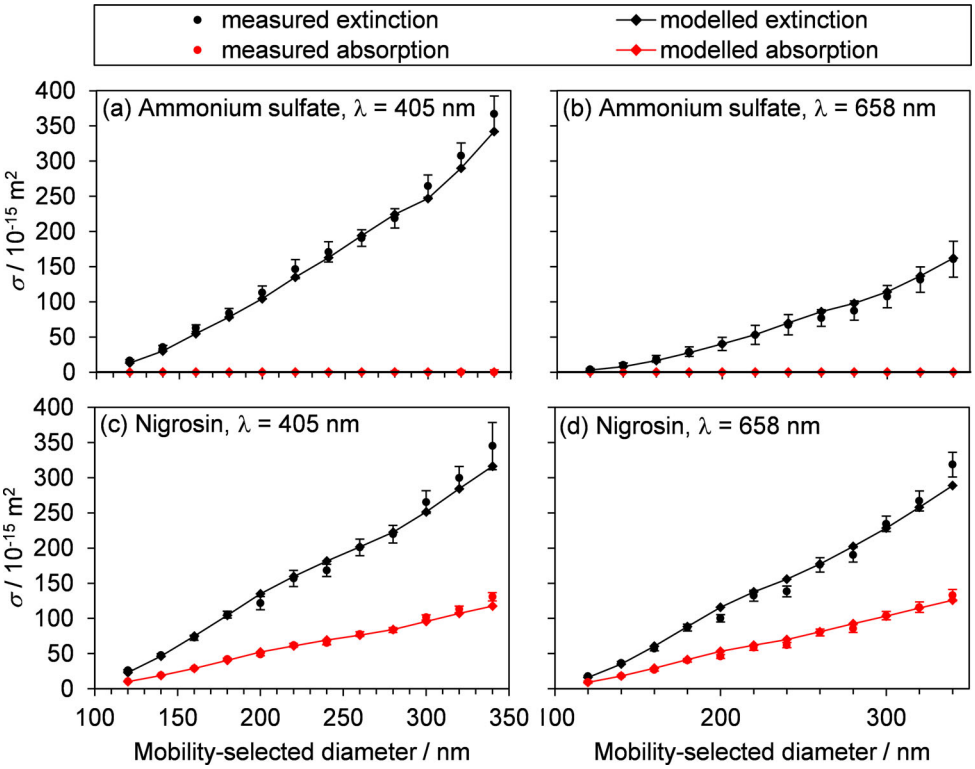

Figure 2. Comparison of measured σ_{ext} and σ_{abs} with model values using the literature RI for (a),(b) AS (Toon et al. 1976), and (c),(d) nigrosin (Bluvshtein et al. 2017). Measurements are shown for both spectroscopy wavelengths of 405 and 658 nm. Vertical error bars represent one standard deviation in the measured cross sections. Lines between model cross section values are to guide the eye only.

formula using $c_+/c_- = 1.0$ and $Z_+/Z_- = 0.957$ as recommended by Tigges et al. (2015b). However, our initial experiments demonstrated poor agreement between measured and predicted cross sections that was not reconciled by considerations of measurement errors in extinction and absorption coefficients, number concentrations, systematic biases in the mobility-selected diameters, or particle losses during the aerosol conditioning and spectroscopic measurement stages. The principal difference between the experimental methods for our previous and current work was the use of different neutralizers and it was clear that our description of the aerosol charge distribution using the Tigges et al. parameterization for a soft x-ray neutralizer was incorrect.

In Section S6, we use a single measurement data set for σ_{ext} at various D_{select} values for an aerosol of known RI (ammonium sulfate) to optimize the aerosol charge distribution model. Briefly, we compared our cross section measurements with model predictions using the methodology described in Section 2.4, with the charge distribution described by the Gunn equation (Equation (5)). We then optimize the ratio c_+Z_+/c_-Z_- in the Gunn equation to minimize the figure of merit χ^2_{ext}. We find that the optimal c_+Z_+/c_-Z_- takes different values for the two different spectroscopy wavelengths, with values of 0.80 and 0.86 found for separate optimisations of 405-nm and 658-nm data. The reasons for differences in the optimal c_+Z_+/c_-Z_- for the two spectroscopy wavelengths are discussed in Section S6 of the SI. These reasons include the fact that we do not recalculate the SMPS-measured size distribution for a new value of c_+Z_+/c_-Z_-, in addition to different size-dependent losses in the flow streams for the two spectroscopy flow lines. While we recognize that ammonium sulfate aerosols do not adopt a true spherical shape, we find no evidence that particle shape is responsible for the differences in c_+Z_+/c_-Z_- for the two spectroscopy wavelengths. Indeed, as we will show in this work, the optimal c_+Z_+/c_-Z_- values provided above provide for excellent closure in aerosol optical properties for nigrosin aerosol that can be considered to have a spherical shape (Lack et al. 2006). In summary, through our optimization procedure, we have effectively calibrated for inaccurate representations of the particle size; we note that previous studies have performed calibrations of extinction data to account for sizing inaccuracies (Toole et al. 2013). In

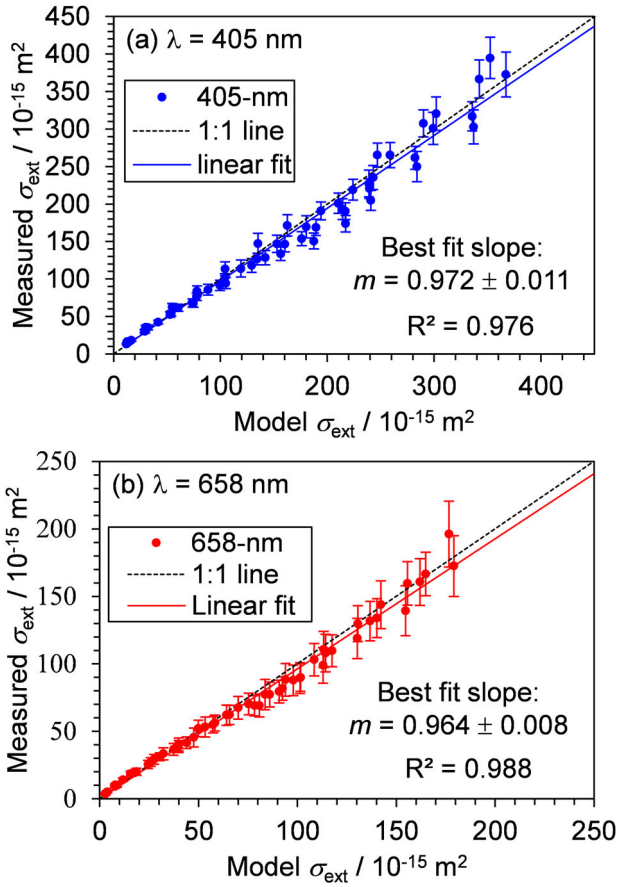

Figure 3. The comparison of the measured and predicted σ_{ext} for five data sets of mobility-selected AS aerosol at optical wavelengths of (a) 405 nm, and (b) 658 nm. Error bars represent one standard deviation in the measured σ_{ext}. Model predictions used the literature RI for AS provided by Toon et al. (1976). The dashed line represents the perfect case of a 1:1 ratio between measured and predicted σ_{ext}. For each wavelength, the slope from a linear regression of the measured versus model cross sections is labeled, with this regression forced through the origin.

all RI retrievals below, we use the aforementioned optimal values for c_+Z_+/c_-Z_- determined for each spectroscopy wavelength.

3. Refractive index retrievals from measured extinction and absorption cross sections

Here, we report measurements of σ_{ext} and σ_{abs} and associated RI retrievals for both non-absorbing (ammonium sulfate, AS) and strongly absorbing (nigrosin) aerosols. We assess the sensitivity and precision of our RI retrievals before reporting retrievals for internally mixed AS-nigrosin aerosols that allow validations of RI mixing rules. We defer an assessment of RI retrieval accuracy to Section 4.

3.1. Ammonium sulfate (non-absorber)

Ammonium sulfate does not absorb light at visible wavelengths and PAS measurements should show no response when the PAS cell is occupied by AS aerosol. Therefore, optical measurements for AS aerosol facilitate assessments of the sensitivities in absorption coefficient (α_{abs}), single scattering albedo (SSA) and the imaginary RI. The AS data sets discussed in this section are different to that used to calibrate for the aerosol charge distribution. For a representative AS data set, Figure 2a,b demonstrates good agreement between measured cross sections with predicted values that use the literature refractive indices reported by Toon et al. (1976) ($n_{405} = 1.540$, $n_{658} = 1.525$ and $k_{405} = k_{658} = 10^{-7}$). We note that this agreement is expected given that we calibrated our aerosol charge distribution such that predicted and measured values of σ_{ext} agreed for an AS calibration data set, but we test our optical measurements for an entirely different aerosol type (light absorbing nigrosin) in the next section. For all five AS data sets, Figure 3a,b compares the measured and predicted σ_{ext} at 405 and 658 nm wavelengths respectively; again, the predicted cross sections use the literature refractive indices reported by Toon et al. (1976). The level of agreement between

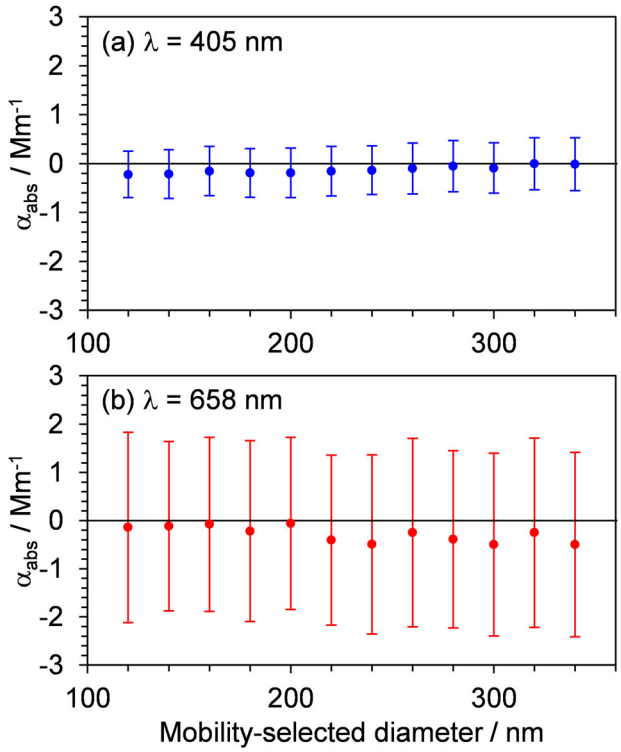

Figure 4. For the same exemplar data set presented in Figure 2 for AS, the variation in the mean absorption coefficient over five-minute sampling for 12 values of D_{select}. Data are shown for measurements by either (a) the 405-nm PAS, or (b) the 658-nm PAS. The 405-nm measurements used an optimized cell designed to suppress the detection of laser-window interactions while the 658-nm measurements used the cell design reported by Lack et al. (2006). Error bars represent one standard deviation in the mean α_{abs}.

the measured and predicted σ_{ext} is quantified from the slopes of a linear regression of the measured versus predicted σ_{ext} data, with the regression forced through the origin. These slopes were determined to be 0.972 ± 0.011 for $\lambda = 405$ nm and 0.964 ± 0.008 for $\lambda = 658$ nm, indicating low levels of bias in the range 3–4% for measured σ_{ext}. This assessment of measurement bias assumes that the n values provided by Toon et al. (1976) for AS are correct which, as we discuss further below, is in agreement with other literature values to within ±0.005.

For the same example data set shown in Figure 2 for AS, Figure 4 shows the variation in the five-minute mean measurements of α_{abs} with D_{select} at the 405 and 658 nm wavelengths. The mean α_{abs} sensitivity characterized from the average standard deviation in α_{abs} for all five AS data sets is 1.02 and 3.23 Mm^{-1} for measurements using the 405-nm and 658-nm PAS cells, respectively. The better sensitivity at the 405 nm wavelength arises partly because these measurements used an optimized PAS cell that suppressed the detection of laser interactions with the cell windows (Cotterell et al. 2019c), while the 658-nm measurements used a common aerosol PAS cell geometry (Lack et al. 2012). Figure S5 in the SI shows the temporal variation in raw absorption coefficients at 405 and 658 nm for a representative AS data set. In (Figure S5 in the SI), the raw absorption coefficient is not background-corrected for the detection of laser-window interactions. The 405-nm absorption (using our optimized cell) is near-zero as expected, while the 658-nm measurements (using the Lack cell) have a large systematic offset in the absorption coefficient of ~70 Mm^{-1} associated with the sensitivity of the Lack cell to laser-window interactions. The signal-to-noise ratio in the microphone response is approximately invariant with signal amplitude. However, when we perform a background subtraction to our measured absorption by subtracting the response when the cell is devoid of any aerosol sample or light absorbing gases, the noise level is not scaled. Therefore, after background subtraction, the signal-to-noise ratio in the 658-nm α_{abs} is approximately three times worse than that in the 405-nm channel. These measurements highlight the importance of using optimal geometry PAS cells to suppress the photoacoustic background for sensitive measurements of aerosol absorption.

We now report RI retrievals for AS, assess the retrieval precision and compare the retrieved values to those in the literature. For each AS data set, we retrieved n and k using the procedure described in

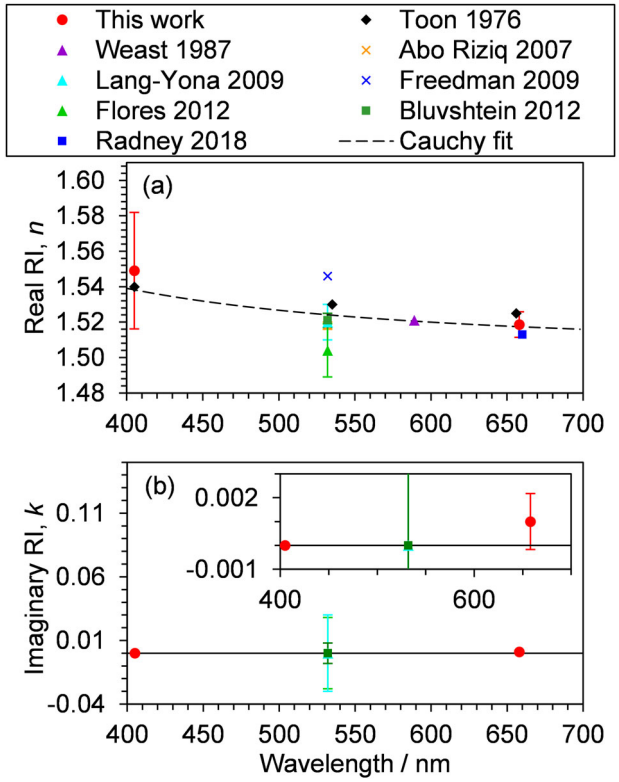

Figure 5. For mobility-selected AS aerosol, our retrieved n and k at 405 and 658 nm wavelengths (red circles) compared to reported values from eight separate literature studies. Literature values include those from Toon et al. (1976), Seinfeld and Pandis (2006) (denoted as 'Weast 1987' in the figure legend), Abo Riziq et al. (2007), Lang-Yona et al. (2009), Freedman et al. (2009), Flores et al. (2012), Bluvshtein et al. (2012) and Radney and Zangmeister (2018). The Cauchy curve in (a) represents the best fit of the Cauchy equation to the literature values for n. The inset in (b) provides an expanded portion of the data to show the uncertainties in our retrieved k values. Vertical error bars for literature data represent the reported uncertainties (when available) in the retrieved values.

Sect. 2.4. For a representative AS data set measured at the 658 nm wavelength, Figure S6 in the SI shows the variation in the merit functions χ^2_{ext}, χ^2_{abs} and χ^2_{total} from fitting the extinction only, absorption only, and extinction and absorption, respectively. This figure clearly demonstrates that k (>0.005) is retrieved incorrectly when fitting σ_{ext} only, while the retrieved n is poorly constrained when fitting σ_{abs} only. However, the retrieval of n and k are both well constrained when fitting both σ_{ext} and σ_{abs} together. This reinforces the conclusion of Zarzana et al. (2014) that the addition of an absorption measurement reduces the retrieval uncertainty.

Figure 5 shows the mean and standard deviation in the retrieved n and k, as determined from all five AS data sets. For n, we retrieve values of $n_{405} = 1.550 \pm 0.033$ and $n_{658} = 1.521 \pm 0.004$, with the uncertainty representing the standard deviation in the n retrieved from each of the five AS data sets. The larger standard deviation in n_{405} is likely associated with the larger uncertainty in the number concentration N_{405} caused by the reliance on transmission factors to convert number concentrations measured by the CPC on the exhaust of the 658-nm PAS channel. Subtle variations in operating conditions (e.g., small changes in the relative flow rates of sample pulled through the 405-nm and 658-nm channels) will affect the value of T_{405}. Moreover, the uncertainty in the ring-down time was 15% lower for the 658-nm CRDS measurements, with relative uncertainties $\Delta\tau/\tau$ measured as 1.91×10^{-3} and 1.63×10^{-3} at the 405 and 658 nm wavelengths, respectively.

Figure 5 also shows several literature RI values for AS. The Cauchy equation describes the wavelength dependence in n for non-absorbing inorganic species over the visible spectrum (Cotterell et al. 2017):

$$n = n_0 + n_1\left[\left(\frac{\lambda_0}{\lambda}\right)^2 - 1\right] \quad (6)$$

in which n_0 is the RI at reference wavelength λ_0 and n_1 is a dispersion coefficient. We fit the Cauchy equation to the literature values plotted in Figure 5. In fitting Equation (6), we set λ_0 to the mid-range wavelength of 550 nm and used a least-squares algorithm to fit n_0 and n_1, with the best-fit coefficients taking values $n_0 = 1.5229$ and $n_1 = 0.0183$. Within

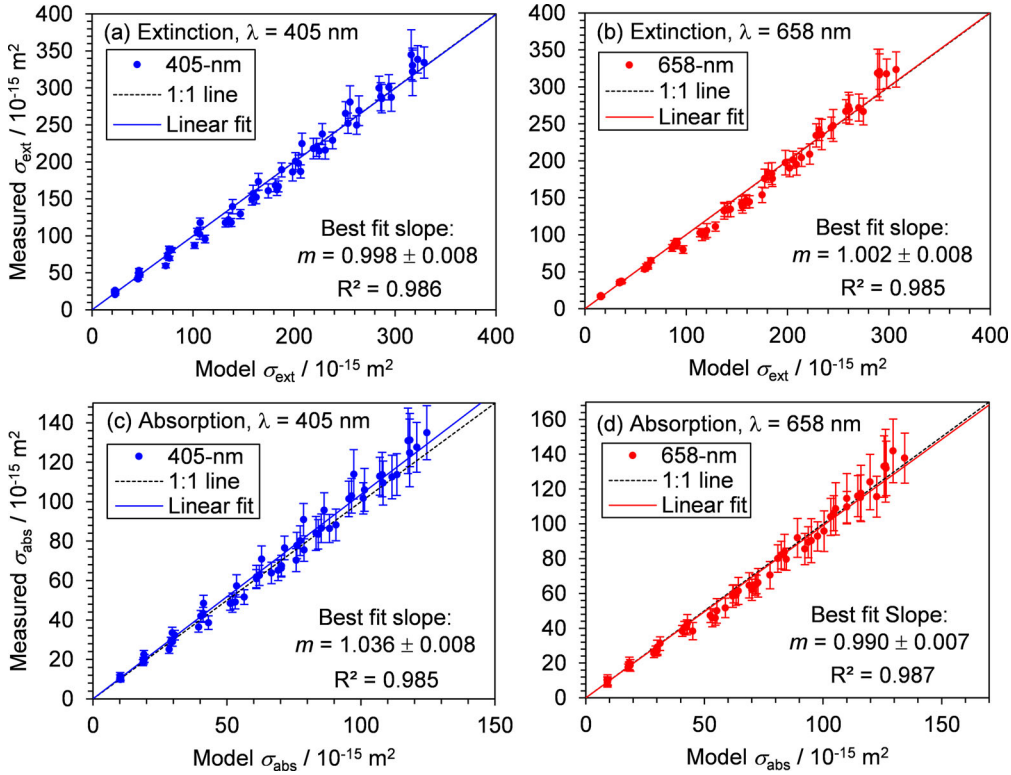

Figure 6. For five data sets of mobility-selected nigrosin aerosol, comparison of the measured and predicted values for σ_{ext} at wavelengths of (a) 405 nm and (b) 658 nm, and for σ_{abs} at wavelengths of (c) 405 nm and (d) 658 nm. Error bars represent one standard deviation in the measured cross sections. Model predictions used the literature refractive indices for nigrosin from Bluvshtein et al. (2017). The dashed line represents the perfect case of a 1:1 ratio between measured and predicted cross sections. The slopes in linear regressions of the measured versus model cross sections are labeled, with this regression forced through the origin.

measurement uncertainty, our retrieved n values agree well with the best-fit Cauchy curve. Compared to the Cauchy fit, our retrieved n_{405} is larger by 0.012 and our retrieved n_{658} larger by 0.004.

For k, we retrieve values of $k_{405} = 0.000 \pm 0.000$ and $k_{658} = 0.001 \pm 0.001$, with the uncertainty representing the standard deviation in k retrieved from each of the five AS data sets. These values are in agreement with AS being a non-absorbing aerosol. The mean value of $k_{568} = 0.001$ might imply small absorption by AS, but this is not the case. Instead, this inaccuracy arises from our choice of varying k by 0.001 in our grid search retrieval algorithm. Future retrievals could use a grid search algorithm with step sizes that vary with the magnitude of k from an initial cycle of fitting. The precision in k_{405} is better than k_{658}, a consequence of the reduced noise in the 405-nm PAS measurements of α_{abs} that use the optimized photoacoustic cell. As we show in Section 4.2, the retrieved k is sensitive to errors in the measured absorption coefficient while the retrieved n has very little dependence on absorption biases. Meanwhile, both n and k are highly sensitive to the measured number particle concentration. In the present case, the absorption by ammonium sulfate at the 405 nm wavelength is measured more precisely and accurately compared to that measured at 658 nm. This absorption uncertainty governs that in the retrieved k, while the retrieved n uncertainty is governed mostly by that in the measured aerosol number concentration which, as we have examined above, is greater for the 405 nm wavelength owing to the CPC location immediately after the 658-nm PAS instrument. Importantly, Figure 5b compares our retrieved values of k with the limited retrieval values reported by other spectroscopy studies, which only used extinction-only methods (Bluvshtein et al. 2012; Flores et al. 2012; Lang-Yona et al. 2009). Figure 5b demonstrates clearly the superior precision in our k retrieval that uses extinction and absorption measurements.

The agreement between our retrieved n and literature values is expected given that we calibrated our aerosol charge distribution such that model and measured values of σ_{ext} agreed for an AS calibration data set. However, the validity of our optimized c_+Z_+/c_-Z_- ratios would be vindicated if excellent optical closure was maintained for an entirely different benchmark

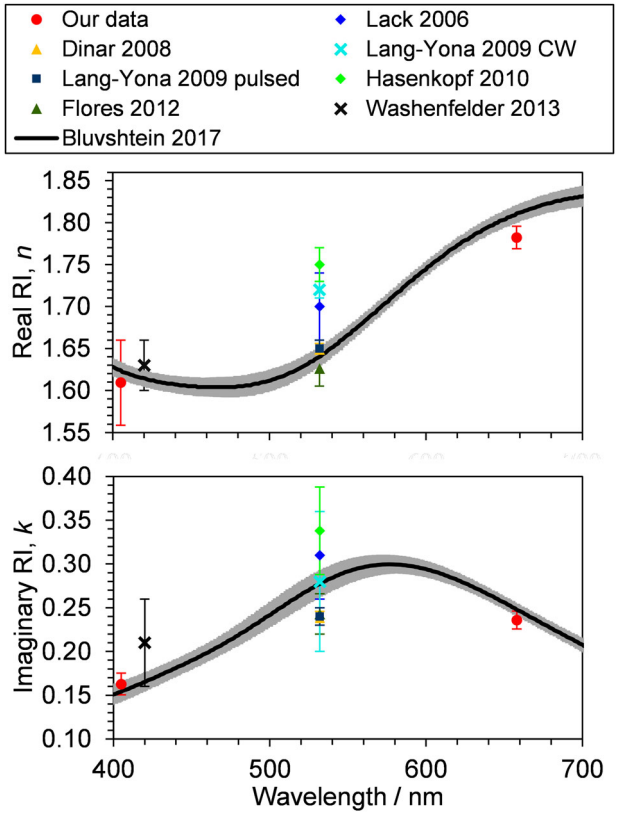

Figure 7. For mobility-selected nigrosin aerosol, our retrieved n and k at 405 and 658 nm wavelengths (red circles) compared to values reported in the literature. Literature values include those from Lack et al. (2006), Dinar et al. (2008), Lang-Yona et al. (2009), Hasenkopf et al. (2010), Flores et al. (2012), Washenfelder et al. (2013), and Bluvshtein et al. (2017). Vertical error bars represent the reported uncertainties (where provided) in the literature values. The gray envelope represents the uncertainty in the spectroscopic ellipsometry retrievals reported by Bluvshtein et al. (2017).

aerosol system, such as a light absorbing organic species, and if closure also held in the PAS-measured absorption. Thus, we now report spectroscopic measurements for mobility-selected nigrosin aerosol.

3.2. Nigrosin (strong absorber)

Figure 2c,d demonstrates agreement between measured and predicted cross sections at 405 and 658 nm wavelengths, respectively, for a representative nigrosin data set. Here, predicted cross sections use literature refractive indices provided by Bluvshtein et al. (2017). For all five nigrosin data sets recorded, Figure 6 compares directly the measured σ_{ext} and σ_{abs} with predicted values at 405 and 658 nm wavelengths; again, the predicted cross sections use the literature refractive indices reported by Bluvshtein et al. (2017). From linear regressions to the measured versus predicted cross sections, with the regression forced through the origin, the slopes for σ_{ext} are 0.998 ± 0.008 and 1.002 ± 0.008 at 405 and 658 nm wavelengths respectively, indicating very low levels of bias ($\sim \pm 0.2\%$). For σ_{abs}, these slopes are 1.036 ± 0.008 and 0.990 ± 0.007 at 405 and 658 nm wavelengths respectively, indicating low levels of bias in the range 1–4%. These low levels of measurement bias are consistent with our measurements reported previously for nigrosin (Davies et al. 2018), further vindicating the use of ozone as a calibrant of aerosol photoacoustic spectrometers at visible wavelengths. We highlight that we have reported previously that ozone calibrations must be performed in a bath gas composed of air for correct calibration of photoacoustic spectrometers at short visible wavelengths, rather than using bath gases of pure N_2 or O_2 (Cotterell et al. 2019a). The aforementioned assessment of measurement bias assumes that the nigrosin RI values provided by Bluvshtein et al. are correct and we discuss below the uncertainties in the intrinsic optical properties of nigrosin associated with potential variability in the composition of nigrosin dye between manufacturers.

We retrieved the RI from each of the five nigrosin data sets using the procedure described in Section 2.4. These retrievals further facilitate our assessments of

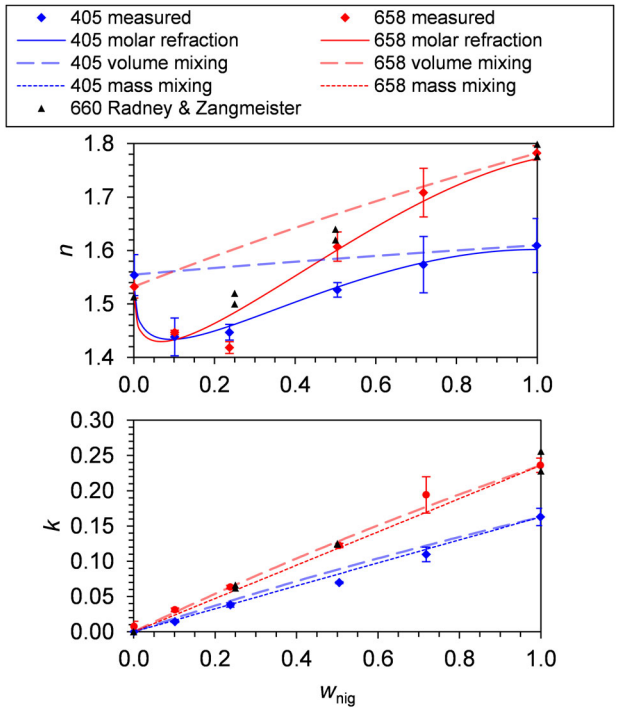

Figure 8. The variation in n and k at 405 and 658 nm wavelengths with w_{nig} for aerosols composed of an internal mixture of AS and nigrosin. Vertical error bars represent one standard deviation in the retrieved values. The black points represent RI values reported by Radney and Zangmeister (2018) at a 660 nm wavelength. Solid lines represent molar refraction mixing rule predictions for n (incorporating aerosol effective density variations reported by Radney and Zangmeister [2018]). Note that the molar refraction mixing rule is shown in the upper plot only, while the mass mixing rule is shown in the lower plot only.

RI retrieval precision. For a representative data set measured at the 658 nm wavelength, Figure S7 shows the dependence of the merit functions χ^2_{ext}, χ^2_{abs} and χ^2_{total} on n and k. This figure shows clearly that k is constrained poorly when minimizing χ^2_{ext} only, the retrieved n is poorly constrained when minimizing χ^2_{abs} only, while the retrieval of n and k are both well constrained when minimizing χ^2_{total}. These observations reinforce the conclusion of Zarzana et al. (2014) that extinction-only retrievals cannot retrieve n or k precisely, while the addition of an absorption measurement improves the retrieval precision.

We retrieved mean RI values of $n_{405} = 1.610 \pm 0.051$, $k_{405} = 0.163 \pm 0.012$, $n_{658} = 1.782 \pm 0.012$ and $k_{658} = 0.236 \pm 0.010$ and these values are plotted on Figure 7. As found for our AS retrievals, the n_{658} precision is better than that for n_{405}, associated with the CPC sampling directly from the exhaust of the 658-nm PAS channel and a 15% lower uncertainty in the 658-nm ring-down times compared to those measured for the 405-nm CRDS. The precisions in the retrieved k_{405} and k_{658} are similar for nigrosin aerosol. Figure 7 compares our retrieved n and k with literature values. All literature values in Figure 7, except those reported by Bluvshtein et al, were retrieved from extinction-only measurements. The spread in past literature retrievals measured at the same wavelength (i.e., at $\lambda = 532$ nm) far exceeds the precision in our RI retrievals. Importantly, the precision in our k retrievals is better than the typical uncertainties in k reported by extinction-only retrievals, in agreement with the expectation that including an absorption measurement constrains the RI retrieval precision and accuracy, particularly for k.

Bluvshtein et al. (2017) measured the n and k for thin films of nigrosin using spectroscopic ellipsometry over the wavelength range 300–800 nm, with their values included in Figure 7. The summed precision and accuracy in the nigrosin refractive indices measured by Bluvshtein et al. are ~0.4% for n and ~5% for k. If we assume the Bluvshtein et al. RI values to be the true values, we can infer the accuracy in our own n and k retrievals. In this way, our RI values differ from the Bluvshtein values by −0.014 (-0.9%), −0.029 (−1.6%), +0.009 (5.8%) and −0.011 (-4.5%) for n_{405}, n_{658}, k_{405} and k_{658}, respectively. However, within the uncertainty of our measurements and those of Bluvshtein et al., all refractive indices agree. This assessment of our RI retrieval accuracy is inappropriate as the optical properties of nigrosin are thought to differ between products from different manufacturers, or indeed between batches from the same manufacturer or for differences in particle generation

conditions (Bluvshtein et al. 2017; Sedlacek and Lee 2007). Nonetheless, we note that both our work and that of Bluvshtein et al. (2017) use water soluble nigrosin produced by Sigma-Aldrich, while the extent of any variation in nigrosin optical properties between manufacturers and batches is not known. Although the good agreement between our RI retrievals with the Bluvshtein values is encouraging, Section 4 reports a rigorous assessment of our retrieval accuracy.

3.3. Refractive indices for internally mixed light absorbing aerosols

A key motivation for measuring aerosol RI is to provide insights into chemical composition. For example, Lambe et al. (2013) and Nakayama et al. (2013) use CRDS and PAS to probe changes in the n and k for secondary organic aerosol with changes in oxidation state. This section reports RI measurements for internally mixed light absorbing aerosols containing known mass fractions of AS and nigrosin. We demonstrate that n and k are measured sensitively with changes in particle composition and we use these measurements to challenge the validity of RI mixing rules applied commonly to internally mixed absorbing aerosols.

We measured the RI for aerosols composed of an internal mixture of AS and nigrosin, with nigrosin mass fractions (w_{nig}) of 0.10, 0.24, 0.50 and 0.72. As described in Section 2.1, aqueous solutions with a solute concentration of 3 g L^{-1} were atomized, and the mass concentrations of AS and nigrosin in the aqueous solution were controlled such that the aforementioned w_{nig} values were achieved in the atomized and dried aerosols. For each w_{nig} value, three measurement data sets were recorded as described in Section 2.1 and the RI was retrieved for each data set. Figure 8 shows the mean n and k with variation in w_{nig}, with the figure also including the measured values reported above for $w_{nig} = 0.0$ (pure AS) and $w_{nig} = 1.0$ (pure nigrosin). Radney and Zangmeister tabulated RI values at a 660 nm wavelength for AS-nigrosin mixtures, but the authors did not consider the underlying physical origin in the observed trends in n and k with w_{nig} (Radney and Zangmeister 2018). Figure 8 shows that our 658-nm retrievals of n and k are in agreement with those reported by Radney and Zangmeister at the 660 nm wavelength.

We used our measured variations in RI to challenge common mixing rules. In the calculations below, we assume that the AS-nigrosin aerosols are homogeneous. Indeed, we have no evidence that would suggest that AS and nigrosin phase separate during the rapid timescale on which the aerosols are dried (~ 1 s), while we show that the RI variations are described well by mixing rules that apply to homogenous particles. Several studies have rigorously challenged mixing rules for the real RI for internally mixed non-absorbing aerosols containing water soluble components (Cai et al. 2016; Cotterell et al. 2015; Liu and Daum 2008). However, little work has challenged mixing rules for internally mixed *light absorbing* aerosols, although we highlight previous work by Abo Riziq et al. (2007) who studied the mixing of AS with Rhodamine 590 dye using an extinction-only retrieval method. Common RI mixing rules include the linear volume fraction and mass fraction mixing rules. We recognize that other effective medium approximations have been developed, such as the Maxwell-Garnett mixing rule, that are sometimes applied in models of aerosol optical properties (Abo Riziq et al. 2007). These effective medium approximations often have their own limitations. For example, the Maxwell-Garnett mixing rule is strictly valid only for small volume fractions of an inclusion within a mixture, while our measurements probed mixtures over a complete mixing range and w_{nig} values ranged from $w_{nig} = 0$ to $w_{nig} = 1$. Moreover, the Maxwell-Garnett and Bruggeman mixing rules use a volume fraction weighting of contributions to the dielectric constant or conductivity, respectively, from each chemical component and ignore the influence of non-ideal chemical interactions between different components on the effective particle density. As we show in this work, accounting for such changes in the effective particle density due to non-ideal chemical interactions between the mixing species can be crucial in predicting the real RI.

For the imaginary RI, Figure 8 shows that k varies linearly with w_{nig} and strongly indicates that a linear mass fraction mixing rule is valid. Therefore, the short-dashed line in Figure 8 represents the predicted variation in effective imaginary RI (k_e) using the mass fraction mixing rule:

$$k_e = \sum_i w_i k_i = w_{nig} k_{nig} + (1 - w_{nig}) k_{AS} \qquad (7)$$

in which the summation is over all i components of the mixture, and w_i and k_i are the mass fraction and imaginary RI of component i, respectively. Here, we replace suffixes i with 'AS' for the ammonium sulfate component and 'nig' for the nigrosin component. Figure 8 shows the mass fraction mixing rule prediction for k_e in which we use our retrieved values for k_{AS} and k_{nig} from Section 3.1 and 3.2 as input values

to Equation (7). The agreement between measured k values and the mass fraction mixing rule is expected as this mixing rule has an underlying physical basis. The imaginary RI is connected to the bulk absorption coefficient ($\alpha_{abs,\,bulk}$) through Equation (8), while $\alpha_{abs,\,bulk}$ is linearly proportional to the mass concentration c_i of the absorbing species through the Beer-Lambert law (with $\alpha_{abs} = \sum_i \varepsilon_i c_i$, in which ε_i is the mass absorption coefficient for the absorbing species).

$$\alpha_{abs,\,bulk} = \frac{4\pi k}{\lambda} \tag{8}$$

It is important to note that Equation (8) is strictly valid for relating *bulk* absorption coefficients to k, while aerosol absorption is a complex function of both k and particle size that requires computation using Mie theory for spherical particles. However, we are *not* using Equation (8) to calculate the aerosol absorption coefficient. Instead, we are recognizing that the imaginary RI is an intrinsic material property and thus k for an aerosol is the same as k for a bulk sample if the aerosol and the bulk sample have the same chemical composition and phase. Crucially, k fundamentally depends on the material composition. Therefore, we can model the dependence of k on the bulk absorption coefficient using Equation (8), and then use the Beer-Lambert law to describe how the bulk absorption coefficient depends on the mass concentration of absorbing species, even though Equation (8) is strictly valid only for bulk samples. For the real RI, Figure 8 shows that the measured n is highly non-linear with variation in nigrosin mass fraction and thus a mass fraction mixing rule is a poor predictor for n_e. Moreover, we find that the volume fraction mixing rule (assuming pure component densities, see below) gives similarly poor predictions for n_e. Therefore, the volume fraction mixing rule is a poor predictor, in agreement with previous studies (albeit on non-absorbing aerosols) that demonstrate that the mass and volume mixing rules are poor predictors for n_e (Cai et al. 2016; Cotterell et al. 2015; Liu and Daum 2008). Instead, the Lorentz-Lorenz equation describes the fundamental connection between n and molecular polarizability, effective density and molecular weight. Therefore, a n_e mixing rule that is self-consistent with the Lorentz-Lorenz relation is required that accounts for the variation in the effective density ρ_e and molecular weight with particle mixing state. The mole fraction (x_i) weighting of molar refraction (the so-called *molar refraction* mixing rule) is self-consistent with the Lorentz-Lorenz relation and is given by (Liu and Daum 2008):

$$R_e = \sum_i x_i R_i = x_{nig} R_{nig} + (1 - x_{nig}) R_{AS} \tag{9}$$

with the molar refraction R related to n via:

$$R = \left(\frac{n^2 - 1}{n^2 + 2}\right)\frac{M}{\rho} \tag{10}$$

in which M is the molecular weight and ρ is the density. Calculations of mole fractions and pure component molar refractions are straightforward. To convert the predicted effective molar refractive R_e from Equation (9) to n_e, we need to describe the variations in the molecular weight (M_e) and effective density (ρ_e) with particle composition. From conservation of mass, M_e is given by:

$$M_e = \sum_i x_i M_i = x_{nig} M_{nig} + (1 - x_{nig}) M_{AS} \tag{11}$$

Meanwhile, Radney and Zangmeister (2018) measured the ρ_e for mixed AS-nigrosin aerosols for w_{nig} values of 0, 0.25, 0.5 and 1.0 using a DMA to control the mobility diameter distribution and an aerosol particle mass analyzer to measure the mass distribution. To parameterize the measured variation in ρ_e with w_{nig}, we used the same empirical parameterization method recommended by Cai et al. (2016) who assessed the accuracy of a range of empirical density parameterisations for approximately 70 organic compounds. Therefore, we fit the polynomial:

$$\rho_e = a + b w_{nig}^{0.5} + c w_{nig} + d w_{nig}^{1.5} \tag{12}$$

in which a, b, c and d are polynomial coefficients. Figure S8 in the SI shows the measured ρ_e from Radney and Zangmeister with variation in $w_{nig}^{0.5}$ and the associated best fit of Equation (12), with best-fit coefficients of $a = 1.730\,\mathrm{g\ cm^{-3}}$, $b = 2.144\,\mathrm{g\ cm^{-3}}$, $c = 4.1971\,\mathrm{g\ cm^{-3}}$ and $d = 2.2981\,\mathrm{g\ cm^{-3}}$. Although there are few data points to constrain the ρ_e parameterization, the parameterized density captures the significant drop in density at small w_{nig} that, as we will show, is important in predicting n_e for internally mixed AS-nigrosin aerosols. We now rationalize the parameterized density variations for the AS-nigrosin mixture. Generally, mixtures of two different chemical species will often have non-ideal chemical interactions that result in deviations in mixture densities from that predicted by simple mass or volume additivity mixing rules. Cai et al. (2016) provide an overview of the impacts of non-ideal interactions on the non-linear variations in density for mixtures of organic components in aqueous aerosols, while Clegg and Wexler (2011) assess the density variations for aqueous salt droplets with the salt concentration. In its pure solid

form, AS adopts an orthorhombic crystal structure at room temperature that has a much higher packing efficiency, and thus a higher density (1.77 g cm^{-3}), compared to that predicted by theoretical models for the corresponding amorphous solid (e.g., density of ~1.5 g cm^{-3}, as shown in Fig. 4(d) of Clegg and Wexler [2011]). Upon internal mixing of AS with a small concentration of nigrosin, the crystal packing is disrupted by the large nigrosin molecules and the density is reduced significantly from the crystalline value for AS. There are large uncertainties in our parameterized effective density variation shown in Figure S8 owing to the very few measurements of the AS-nigrosin mixture density reported in the literature. Nonetheless, the parameterization captures a sharp drop in particle density as nigrosin is added to the particle, consistent with our expectations when considering the aforementioned impact of large organic molecules on the crystalline packing of AS.

In calculations of n_e using the molar refraction mixing rule using the procedure described above, we used the pure component n_{AS} and n_{nig} values determined in 3.1 and 3.2. To calculate the pure component molar refractivities R_{AS} and R_{nig}, we used the known densities for AS (1.77 g cm^{-3}, Haynes [2015]) and nigrosin (1.50 g cm^{-3}, Radney and Zangmeister [2018]). We take molecular weights of $M_{AS} = 132$ g mol^{-1} and $M_{nig} = 922$ g mol^{-1}, although we note that the molecular weight of nigrosin is highly uncertain with various values reported in the range 753 – 1091 g mol^{-1} (Hasenkopf et al. 2010; Lack et al. 2006) and we take a mid-range value. We highlight that the exact values of the pure component molecular weights are unimportant when calculating n_e variations in the mass fraction domain as the molecular weight terms cancel. The solid lines in Figure 8 show our molar refraction mixing rule predictions for n_e at 405 and 658 nm wavelengths with variation in w_{nig}, clearly demonstrating good agreement with our measured RI values. Importantly, the molar refraction mixing rule predicts correctly a decrease in n_e on addition of small nigrosin concentrations to AS and this decrease is associated with a reduction in particle density. Our measurements demonstrate the strong relationship between n_e and particle density, with the latter quantity related in a non-linear and non-ideal way to the particle composition, and ideal mixing treatments of aerosol density fail to capture important changes in ρ_e with composition variation that impact strongly on n_e.

In the knowledge that our molar refraction mixing rule, when combined with a correct description of ρ_e, accurately predicts n_e for AS-nigrosin mixtures and that we validated published wavelength-dependent RI values for pure AS and nigrosin in Sections 3.1 and 3.2 respectively, we now calculate n_e with variation in both particle composition and wavelength. For these calculations, we used our Cauchy description of n_{AS} over the 400 – 700 nm wavelength range (see Figure 5), and the Bluvshtein et al. (2017) description of n_{nig} over the same wavelength range (see Figure 7). Similarly, we demonstrated that the mass fraction mixing rule predicts *accurately* k_e for AS-nigrosin mixtures and we can calculate k_e with variation in both nigrosin mass fraction and wavelength, using $k_{AS} = 0$ and the k_{nig} reported by Bluvshtein et al. (2017). Figure S9 (in the SI) shows the calculated n_e and k_e with variation in both wavelength and nigrosin mass fraction and further highlights the non-linear and non-monotonic nature of n_e variations in the two important domains of wavelength and particle composition. Given the use of mixing rules in relating aerosol optical properties to chemical composition and in predicting aerosol radiative impacts (Erlick et al. 2011), it is important that researchers use accurate mixing rules for predicting refractive indices. The work presented here demonstrates that the common volume fraction mixing rule fails to describe refractive indices accurately for internally mixed light absorbing aerosols. We highlight that the RI of AS is often used in radiative forcing calculations for marine aerosol and we have shown here that only small concentrations of impurities are needed to reduce n_e significantly for AS-containing aerosols, a phenomenon that is not captured by the volume fraction mixing rule. More assessments are needed to ascertain what mixing rules and optical interaction models are most appropriate for a given aerosol composition and structure. For example, the mixing rules assessed here assume that the particles are homogeneously internally mixed, as expected to be achieved in our measurements based on the high water solubility of both AS and nigrosin. However, other components of aerosols of great importance to atmospheric optics, such as black carbon, are insoluble in water and the mixing of chemical species with black carbon is often highly inhomogeneous (e.g., see Fig. 4 of Li et al. 2016). Indeed, while RI mixing is an important consideration, so is the judicious choice of the optical scattering-absorption model (e.g., Mie Theory, Core-Shell Mie Theory, Core Gray Shell model, T-Matrix, etc., see Kahnert and Kanngießer (2020)).

4. Accuracy of refractive index retrievals from measured extinction and absorption cross sections

Sections 4.1 and 4.2 assessed the precision and sensitivity in our RI retrievals. While it was encouraging

that our retrieved n and k for AS or nigrosin aerosols agreed well with literature values, this section provides a rigorous assessment of the how measurement biases affect the RI retrieval accuracy.

Miles et al. (2010) assessed the sensitivity in retrieved n from extinction-only measurements for mobility-selected non-absorbing aerosols, considering a range of measurement biases including those in the relative fraction of the CRDS optical path occupied by aerosol (see Section S1), aerosol number concentrations, size distribution and corrections for multiply charged particles. For RI retrievals from σ_{ext} and σ_{abs} for mobility-selected non-absorbing or absorbing aerosols, Zarzana et al. (2014) used a Monte Carlo analysis to assess the accuracy in n and k arising from systematic errors of ±5% in the measured α_{ext}, α_{abs} and in a correction constant to account for the presence of doubly charged particles only. Zarzana et al. (2014) acknowledge that their accuracy assessments were best-case scenarios, with several error sources, including those in the CPC counting and size distribution measurements, neglected. In particular, the authors did not account correctly for the impact of multiply charged particles; as we discussed in Section 2.4, particles with n_e up to $n_e = 6$ impact significantly on measured cross sections. Browne et al. (2019) also performed a Monte Carlo analysis to determine the accuracy in n and k retrievals from CRDS and PAS measurements of σ_{ext} and σ_{abs}, albeit for full distribution measurements that did not use any methods for mobility or size selection. The authors considered normally distributed uncertainties in the measured α_{ext}, α_{abs} and size distribution with associated standard deviations of ±4%, ±8% and ±10%, respectively, for optical measurements at 405 and 532 nm wavelengths. Here, we assess our RI retrieval accuracies, considering the complete range of measurement biases that affect the retrieval for mobility-selected aerosol. Section 4.2 presents an error sensitivity study that assesses the impact of specific measurement biases on the RI retrieval accuracy, then Section 4.3 reports the likely retrieval accuracies arising from the combination of several measurement biases using a Monte Carlo analysis. First, we discuss the sources and magnitudes of bias in our measurements.

4.1. Sources and magnitudes of measurement bias

Our σ_{ext} and σ_{abs} are calculated from measured extinction and absorption coefficients and CPC-measured aerosol number concentrations. Meanwhile, our model cross section predictions use a particle size distribution for the mobility-selected aerosol that depends on the aerosol charge distribution, the DMA transfer function and the SMPS-measured size distribution input to the DMA. Table 1 summarizes the sources of bias in our RI retrievals. Other uncertainties not included in Table 1, but expected to have a negligible impact on the retrieval, are those in the laser wavelength and in the measured ring-down time. The uncertainties in the measured laser wavelengths are ±1.0 nm. Meanwhile, errors in the ring-down time may arise from the presence of gaseous absorbers, although our measurements use zero air gas, a carbon-based scrubber to remove trace NO_2 and O_3, and several stages of drying to remove water vapor. Moreover, measurement of the particle-free ring-down time (τ_0) before and after the mobility-selection time intervals provides an effective correction for the impact of gaseous absorbers if the gas absorber concentration remains constant over the data set measurement period. We measured τ_0 to be invariant over a given day, with fluctuations in τ_0 corresponding to variation in the extinction coefficient by 3 Mm^{-1} at most. Section S11 describes how we used our own measurements and published data to assign appropriate bias magnitudes to each source of bias in Table 1. Briefly, the CRDS-measured extinction coefficient depends on the ratio (R_L) of the cavity length occupied by aerosol sample to the geometric length between the two cavity mirrors and we find that R_L has a potential bias of up to 0.0173, corresponding to a 1.5% bias. Both the CPC-measured number concentration and the PAS-measured absorption have associated measurement biases of 5%, with the bias in absorption coefficient arising mostly from the accuracy in the PAS calibration. The ratio c_+Z_+/c_-Z_- that governs the aerosol charge distribution has different biases associated with it depending on the spectroscopy wavelength; we estimate biases in c_+Z_+/c_-Z_- of 0.08 and 0.02 at the 405 and 658 nm spectroscopy wavelengths, respectively. The aerosol flow rate has an associated bias of up to 10%, while the diameter in SMPS-measured size distributions has an associated uncertainty of 3.66%.

4.2. Sensitivity of refractive index retrievals to measurement biases

We assessed the sensitivity of the retrieved n and k to measurement biases for pure scattering (AS) or strongly absorbing (nigrosin) aerosols. In this sensitivity analysis, we apply positive biases to measured quantities. For each source of measurement bias, the

Table 1. A summary of the sources and magnitudes of measurement bias considered in our RI retrieval accuracy assessment, and their associated impacts on the retrieval accuracies Δn and Δk for $\lambda = 405$, 658 nm and for both non-absorbing (AS) and absorbing (nigrosin) aerosol. The numbers in brackets represent the accuracies as a percentage.

		Non-absorber (AS)				Strong absorber (nigrosin)			
Source of error	Bias magnitude	Δn_{405}	Δk_{405}	Δn_{658}	Δk_{658}	Δn_{405}	Δk_{405}	Δn_{658}	Δk_{658}
Relative length of the CRDS cavity occupied by aerosol, R_L	0.0173 (1.5%)	0.007 (0.4%)	0.000	0.004 (0.3%)	0.000	0.011 (0.7%)	−0.002 (−1.4%)	0.014 (0.8%)	−0.003 (−1.2%)
PAS calibration coefficient	5%	0.000	0.000	0.000	0.000	0.002 (0.1%)	0.016 (9.1%)	−0.006 (−0.4%)	0.022 (8.6%)
CPC number concentration, N_{CPC}	5%	−0.021 (−1.4%)	0.000	−0.014 (−1.0%)	0.000	−0.038 (−2.4%)	−0.008 (−4.9%)	−0.039 (−2.2%)	−0.012 (−5.3%)
c_+Z_+/c_Z	0.08 (λ = 405 nm)	−0.036 (−2.4%)	0.000	−0.009 (−0.6%)	0.000	−0.055 (−3.6%)	−0.013 (−8.5%)	−0.015 (−0.9%)	−0.006 (−2.5%)
	0.02 (λ = 658 nm)								
Aerosol flow rate through DMA column	10%	0.000 (0.0%)	0.000	−0.001 (−0.1%)	0.000	−0.001 (0.0%)	0.000 (0.0%)	−0.001 (0.0%)	0.000 (0.0%)
Particle diameter in SMPS size distribution measurements, D_{SMPS}	3.66%	−0.014 (−0.9%)	0.000	−0.018 (−1.2%)	0.000	−0.023 (−1.5%)	−0.004 (−2.6%)	−0.036 (−2.1%)	−0.007 (−3.0%)

associated bias magnitude was applied and the RI was retrieved for a data set. This retrieval was repeated for all five data sets recorded for a given aerosol species and the mean RI values (denoted $\overline{n'}$ and $\overline{k'}$) for all five data sets were calculated. We then calculated the differences between these mean RI values and those for the unperturbed ($\bar{n}$ and $\bar{k}$) data sets using:

$$\begin{aligned} \Delta n &= \bar{n}' - \bar{n} \\ \Delta k &= \bar{k}' - \bar{k} \end{aligned} \tag{13}$$

Table 1 summarizes the calculated errors Δn and Δk for each source of measurement bias. For AS, k is not affected by sources of measurement bias as the absorption cross section is consistently measured to be near-zero (see Figure 4 for measurements of absorption coefficient) such that k is constrained to an accuracy better than 0.001, i.e., the step in k used in our grid search retrieval. The accuracy in the retrieved n is most sensitive to biases in c_+Z_+/c_Z and N_{CPC}, with associated Δn of 2.4% and 1.4% at the 405 nm wavelength. The impact of c_+Z_+/c_Z on Δn is larger at the 405 nm wavelength due to the larger corresponding bias in c_+Z_+/c_Z. At both wavelengths, the sensitivity in Δn to biases in the SMPS particle diameter is ∼1%. The impact of uncertainty in R_L on the retrieval accuracy is very small, while changes in the aerosol flow rate have no impact on the retrieval. For nigrosin, biases in c_+Z_+/c_Z, the PAS calibration coefficient and N_{CPC} all have strong impacts on the retrieved n and k. Notably, the 5% measurement bias in the PAS calibration coefficient introduces an error of ∼9% in the retrieved k at both wavelengths. Again, the impact of bias in R_L and aerosol flow rate have very little impact on the retrieved RI.

4.3. Monte Carlo assessment of refractive index retrieval accuracy

While our sensitivity analysis is useful in assessing which sources of measurement bias impact most on the RI retrieval accuracy, the overall retrieval accuracy depends on the *combination* of measurement biases. Here, we perform a Monte Carlo analysis that repeats RI retrievals for hundreds of different combinations of randomly distributed measurement biases. To ensure we achieve a statistically representative combination of errors for the most significant measurement biases within the computational power we have available, we ignore the impact of R_L and aerosol flow rate uncertainties that have only a small impact on the retrieval accuracy. Furthermore, we performed our Monte Carlo calculations on only single data sets for either AS or nigrosin, choosing representative data sets for

AS or nigrosin aerosol. There was no methodology used to pick a representative data set, as our measurement data sets all shown a high degree of consistency. We retrieved the n and k for each data set with different combinations of measurement bias for the PAS calibration coefficient, aerosol number concentrations, c_+Z_+/c_-Z and the SMPS diameter. For a given retrieval, the bias values for each of these four sources were assigned randomly to a value in-between the positive and negative values of the corresponding bias magnitudes summarized in Table 1 (e.g., a value from –5% to +5% for the PAS calibration coefficient). We repeated this retrieval for 200 combinations of randomly combined biases. We chose to apply randomly-distributed bias amplitudes because we do not have accurate assessments of the probability distributions for our measurement biases that would allow us to represent our bias distributions with Gaussian distributions. However, we note that similar Monte Carlo analyses have chosen to normally distribute measurement biases which subsequently reduce the range of retrieved refractive indices significantly (Browne et al. 2019). Therefore, the true accuracies in our RI retrievals are likely better than the estimates we report.

Figures S11–S14 in the SI show the random bias distributions applied to the PAS calibration coefficient, aerosol number concentration, c_+Z_+/c_-Z and the SMPS diameter for each wavelength and for AS or nigrosin data sets. Figure 9 summarizes the retrieved distributions for n and k. As expected, the probability distributions in the applied biases are random and resemble a top hat distribution, while the retrieved n and k are normally distributed. We fit the retrieved n and k to normal distributions to determine the means and standard deviations in these distributions, with the standard deviations in n and k (δ_n and δ_k, respectively) characterizing the accuracies in the retrieved values. For n, we find that δ_n is $<$2% for AS and $<$3% for nigrosin. The accuracy in k depends strongly on the absorption strength. In the limit of no absorption, δ_k takes a value of 0.000 for AS. In the limit of strong absorption, δ_k is ~8% for nigrosin and is worse than the 2% error in k estimated previously by Zarzana et al. (2014) through a Monte Carlo analysis. However, our analysis accounts for a more comprehensive range of errors than considered in previous work. Moreover, we stress that our Monte Carlo estimates for δ_n and δ_k are upper estimates as we describe the measured biases using a random distribution, while these biases are likely normally distributed. Nonetheless, the accuracies in n and k are sufficient to allow us to investigate variations in RI with composition and wavelength, such as in our study for internally mixed light absorbing aerosol reported in Section 3.3.

5. Summary

This work investigated RI retrievals from CRDS and PAS measurements on mobility-selected aerosol at wavelengths of 405 and 658 nm. We reported RI retrievals for AS aerosol (a non-absorber) and nigrosin aerosol (a strong light absorber) and find good agreement between our retrievals with those reported previously in the literature. We used our measurements to assess the precision and sensitivity in our RI retrievals. For non-absorbing AS, we measured n_{405} and n_{658} to a precision of 2.1% and 0.3%, respectively, while k was retrieved to a precision of better than 0.001, i.e., to within the step size for k used in our grid-search fit routine. For light-absorbing nigrosin, we measured n_{405}, n_{658}, k_{405}, and k_{658} to a precision of 3.2%, 0.7%, 7.4%, and 4.2%, respectively. The better precision in the 658-nm retrievals are associated with reduced uncertainty in aerosol number concentrations for the spectrometers at this wavelength (with the CPC sampling directly from the exhaust of the 658-nm PAS channel) and a 15% lower uncertainty in the 658-nm ring-down times compared to those measured for the 405-nm CRDS. In addition, we used a Monte Carlo error propagation analysis to quantify upper limit values for our retrieval accuracies. This analysis is the first to account for the full range of measurement uncertainties involved in RI retrievals from optical measurements on mobility-selected aerosol. We assess that the accuracy in n is in the range 2–3%, while the accuracy in k is strongly dependent on absorption strength with an accuracy better than 0.001 for non-absorbing aerosol and better than 8% for strongly absorbing (nigrosin) aerosols. We also report the first experimental validation of predictive RI mixing rules for non-aqueous internally mixed light absorbing aerosols by comparing the n and k from predictive mixing rules with measured values for aerosol composed of an internal mixture of ammonium sulfate and nigrosin dye. The variation in imaginary RI with chemical composition is captured by a mass fraction mixing rule, while the variation in the real RI is correctly predicted by a molar refraction mixing rule when combined with accurate values for effective aerosol density. Meanwhile, the commonplace volume fraction mixing rule fails to predict refractive indices accurately for internally mixed light absorbing aerosols and mixing rules with a physical basis must

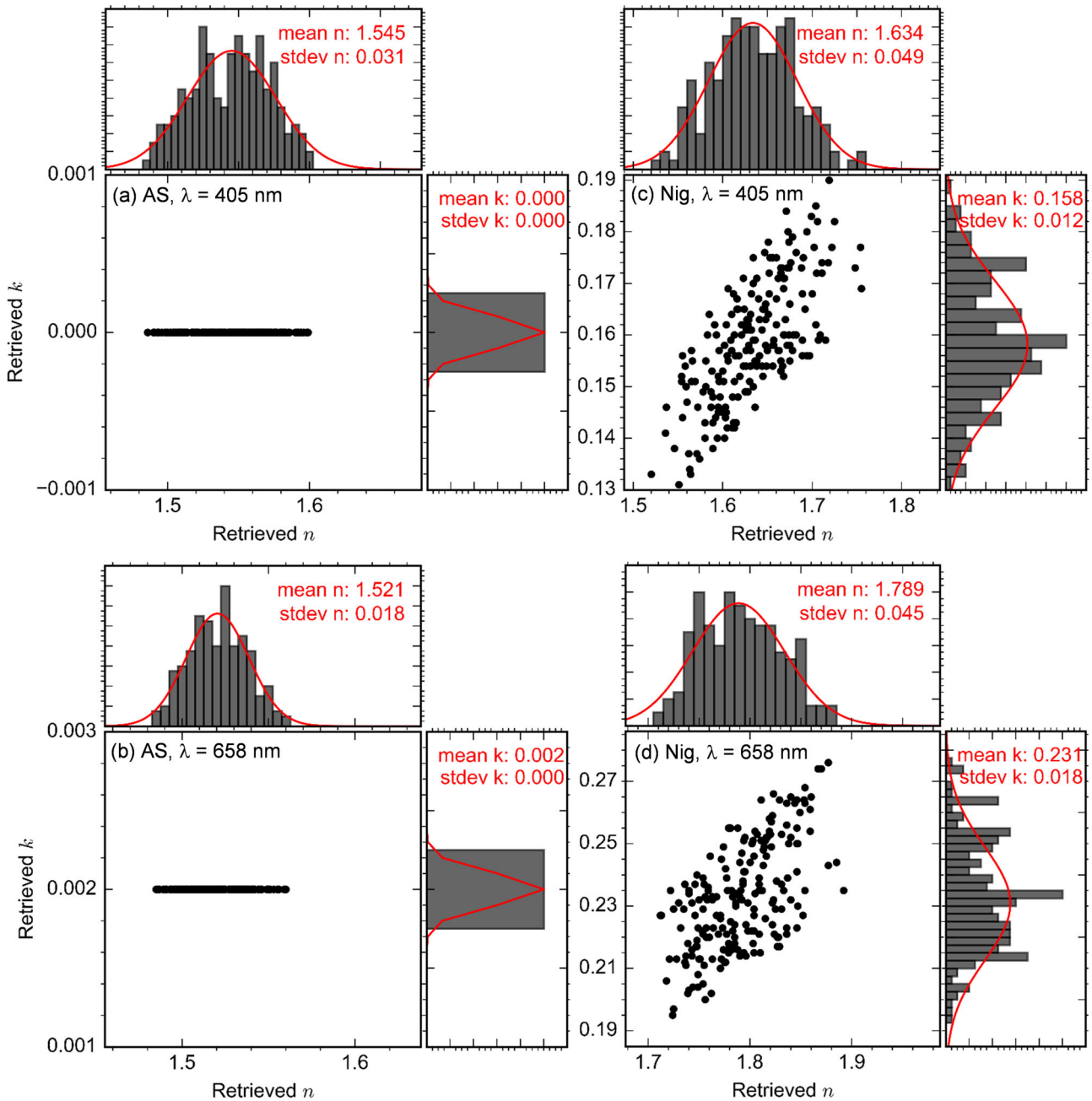

Figure 9. Scatter plots summarizing the Monte Carlo error analysis for RI retrievals at both 405 and 658 nm wavelengths and for aerosols composed of (a), (b) AS, and (c), (d) nigrosin. Each scatter plot shows the corresponding histogram distributions for the retrieved *n* and *k*, with these distributions fit to a Gaussian distribution to determine the mean and standard deviation in the retrievals.

be used. We emphasize that the RI of AS is often used in radiative forcing calculations for marine aerosol and we have shown here that only small concentrations of impurities are needed to reduce n_e significantly for AS-containing aerosols, a phenomenon that is not captured by a linear volume fraction mixing rule. Finally, aerosol particles have variable, and often highly complex, mixing states and structures. This work has validated mixing rules for well-mixed homogeneous spherical particles and predicting optical properties accurately for other aerosol particle types will require different optical models and mixing rules.

Acknowledgments

The Met Office funded this work. Michael I. Cotterell and Jim M. Haywood thank the Natural Environment Research Council for support through the CLARIFY-2017 grant (NE/L013797/1). Jim M. Haywood was also part funded for this

research by the SASSO grant (NE/S00212X/1). Michael I. Cotterell acknowledges support from the Royal Society of Chemistry/Analytical Chemistry Trust Fund through a Tom West Fellowship. The Research Council on Norway provided further instrument support via the projects AC/BC (240372) and NetBC (244141).

Data availability

For data related to this article, please contact Michael I. Cotterell (m.cotterell@bristol.ac.uk).

Competing interests

The authors declare that they have no conflict of interest.

ORCID

Michael Cotterell: 0000-0001-5533-7856

References

Abo Riziq, A.,. C. Erlick, E. Dinar, and Y. Rudich. 2007. Optical properties of absorbing and non-absorbing aerosols retrieved by cavity ring down (CRD) spectroscopy. *Atmos. Chem. Phys.* 7 (6):1523–36. doi:10.5194/acp-7-1523-2007.

Alexander, N., S. Allen, T. F. Stocker, D. Qin, G.-K. Plattner, M. M. B. Trignor, J. Boschung, Y. Xia, V. Bex, and P. M. Midgley. 2013. Working Group I Contribution to the Fifth Assessment Report of the Intergovernmental Panel on Climate Change.

Banerjee, S., and R. N. Zare. 2015. Syntheses of Isoquinoline and Substituted Quinolines in Charged Microdroplets. *Angew. Chem. Int. Ed.* 54 (49):14795–9. doi:10.1002/anie.201507805.

Banerjee, S., E. Gnanamani, X. Yan, and R. N. Zare. 2017. Can all bulk-phase reactions be accelerated in microdroplets? *Analyst* 142 (9):1399–402. doi:10.1039/C6AN02225A.

Bluvshtein, N., J. M. Flores, A. A. Riziq, and Y. Rudich. 2012. An approach for faster retrieval of aerosols' complex refractive index using cavity ring-down spectroscopy. *Aerosol Sci. Technol* 46 (10):1140–50. doi:10.1080/02786826.2012.700141.

Bluvshtein, N., J. M. Flores, Q. He, E. Segre, L. Segev, N. Hong, A. Donohue, J. N. Hilfiker, and Y. Rudich. 2017. Calibration of a multi-pass photoacoustic spectrometer cell using light-absorbing aerosols. *Atmos. Meas. Tech.* 10 (3):1203–13. doi:10.5194/amt-10-1203-2017.

Bluvshtein, N., J. Michel Flores, L. Segev, and Y. Rudich. 2016. A new approach for retrieving the UV–vis optical properties of ambient aerosols. *Atmos. Meas. Tech.* 9 (8):3477–90. doi:10.5194/amt-9-3477-2016.

Browne, E. C., X. Zhang, J. P. Franklin, K. J. Ridley, T. W. Kirchstetter, K. R. Wilson, C. D. Cappa, and J. H. Kroll. 2019. Effect of heterogeneous oxidative aging on light absorption by biomass burning organic aerosol. *Aerosol Sci. Technol* 53 (6):663–74. doi:10.1080/02786826.2019.1599321.

Cai, C.,. D. J. Stewart, T. C. Preston, J. S. Walker, Y.-H. Zhang, and J. P. Reid. 2014. A new approach to determine vapour pressures and hygroscopicities of aqueous aerosols containing semi-volatile organic compounds. *Phys. Chem. Chem. Phys.* 16 (7):3162–72. doi:10.1039/c3cp54948h.

Cai, C.,. R. E. H. Miles, M. I. Cotterell, A. Marsh, G. Rovelli, A. M. J. Rickards, Y. Zhang, and J. P. Reid. 2016. Comparison of methods for predicting the compositional dependence of the density and refractive index of organic–aqueous aerosols. *J. Phys. Chem. A* 120 (33):6604–17. doi:10.1021/acs.jpca.6b05986.

Clegg, S. L., and A. S. Wexler. 2011. Densities and Apparent Molar Volumes of Atmospherically Important Electrolyte Solutions. 1. The Solutes H_2SO_4, HNO_3, HCl, Na_2 SO_4, $NaNO_3$, NaCl, $(NH_4)_2$ SO_4, NH_4 NO_3, and NH_4Cl from 0 to 50 °C, Including Extrapolations to Very Low Tempe. *J. Phys. Chem. A* 115 (15):3393–460. doi:10.1021/jp108992a.

Cotterell, M. I., A. J. Orr-Ewing, K. Szpek, J. M. Haywood, and J. M. Langridge. 2019a. The impact of bath gas composition on the calibration of photoacoustic spectrometers with ozone at discrete visible wavelengths spanning the Chappuis band. *Atmos. Meas. Tech.* 12 (4):2371–85. doi:10.5194/amt-12-2371-2019.

Cotterell, M. I., B. J. Mason, T. C. Preston, A. J. Orr-Ewing, and J. P. Reid. 2015. Optical extinction efficiency measurements on fine and accumulation mode aerosol using single particle cavity ring-down spectroscopy. *Phys. Chem. Chem. Phys.* 17 (24):15843–56. doi:10.1039/C5CP00252D.

Cotterell, M. I., G. P. Ward, A. P. Hibbins, A. Wilson, J. M. Haywood, and J. M. Langridge. 2019c. Optimizing the performance of aerosol photoacoustic cells using a finite element model. Part 2: Application to a two-resonator cell. *Aerosol Sci. Technol* 53 (10):1128–48. doi:10.1080/02786826.2019.1648749.

Cotterell, M. I., G. P. Ward, A. P. Hibbins, J. M. Haywood, A. Wilson, and J. M. Langridge. 2019b. Optimizing the performance of aerosol photoacoustic cells using a finite element model. Part 1: Method validation and application to single-resonator multipass cells. *Aerosol Sci. Technol* 53 (10):1107–27. doi:10.1080/02786826.2019.1650161.

Cotterell, M. I., R. E. Willoughby, B. R. Bzdek, A. J. Orr-Ewing, and J. P. Reid. 2017. A complete parameterisation of the relative humidity and wavelength dependence of the refractive index of hygroscopic inorganic aerosol particles. *Atmos. Chem. Phys.* 17 (16):9837–51. doi:10.5194/acp-17-9837-2017.

Cotterell, M. I., T. C. Preston, A. J. Orr-Ewing, and J. P. Reid. 2016. Assessing the accuracy of complex refractive index retrievals from single aerosol particle cavity ring-down spectroscopy. *Aerosol Sci. Technol* 50 (10):1077–95. doi:10.1080/02786826.2016.1219691.

Davies, N. W., C. Fox, K. Szpek, M. I. Cotterell, J. W. Taylor, J. D. Allan, P. I. Williams, J. Trembath, J. M. Haywood, and J. M. Langridge. 2019. Evaluating biases in filter-based aerosol absorption measurements using photoacoustic spectroscopy. *Atmos. Meas. Tech.* 12 (6):3417–34. doi:10.5194/amt-12-3417-2019.

Davies, N. W., M. I. Cotterell, C. Fox, K. Szpek, J. M. Haywood, and J. M. Langridge. 2018. On the accuracy of

aerosol photoacoustic spectrometer calibrations using absorption by ozone. *Atmos. Meas. Tech.* 11 (4):2313–24. doi:10.5194/amt-11-2313-2018.

De Haan, D. O., L. N. Hawkins, H. G. Welsh, R. Pednekar, J. R. Casar, E. A. Pennington, A. de Loera, N. G. Jimenez, M. A. Symons, M. Zauscher, et al. 2017. Brown carbon production in ammonium- or amine-containing aerosol particles by reactive uptake of methylglyoxal and photolytic cloud cycling. *Environ. Sci. Technol.* 51 (13): 7458–66. doi:10.1021/acs.est.7b00159.

Dinar, E., A. Abo Riziq, C. Spindler, C. Erlick, G. Kiss, and Y. Rudich. 2008. The complex refractive index of atmospheric and model humic-like substances (HULIS) retrieved by a cavity ring down aerosol spectrometer (CRD-AS). *Faraday Discuss* 137:279–95. doi:10.1039/B703111D.

Erlick, C., J. P. D. Abbatt, and Y. Rudich. 2011. How different calculations of the refractive index affect estimates of the radiative forcing efficiency of ammonium sulfate aerosols. *J. Atmos. Sci.* 68 (9):1845–52. doi:10.1175/2011JAS3721.1.

Fischer, D., and G. D. Smith. 2018. A portable, four-wavelength, single-cell photoacoustic spectrometer for ambient aerosol absorption. *Aerosol Sci. Technol* 52 (4):393–406. doi:10.1080/02786826.2017.1413231.

Flores, J. M., D. F. Zhao, L. Segev, P. Schlag, A. Kiendler-Scharr, H. Fuchs, Å. K. Watne, N. Bluvshtein, T. F. Mentel, M. Hallquist, et al. 2014. Evolution of the complex refractive index in the UV spectral region in ageing secondary organic aerosol. *Atmos. Chem. Phys.* 14 (11): 5793–806. doi:10.5194/acp-14-5793-2014.

Flores, J. M., R. Z. Bar-Or, N. Bluvshtein, A. Abo-Riziq, A. Kostinski, S. Borrmann, I. Koren, I. Koren, and Y. Rudich. 2012. Absorbing aerosols at high relative humidity: linking hygroscopic growth to optical properties. *Atmos. Chem. Phys.* 12 (12):5511–21. doi:10.5194/acp-12-5511-2012.

Foster, K., R. Pokhrel, M. Burkhart, and S. Murphy. 2019. A novel approach to calibrating a photoacoustic absorption spectrometer using polydisperse absorbing aerosol. *Atmos. Meas. Tech.* 12 (6):3351–63. doi:10.5194/amt-12-3351-2019.

Freedman, M. A., C. A. Hasenkopf, M. R. Beaver, and M. A. Tolbert. 2009. Optical properties of internally mixed aerosol particles composed of dicarboxylic acids and ammonium sulfate. *J. Phys. Chem. A* 113 (48): 13584–92. doi:10.1021/jp906240y.

Fuchs, N. A. 1963. On the stationary charge distribution on aerosol particles in a bipolar ionic atmosphere. *Geofis. Pura e Appl* 56 (1):185–93. doi:10.1007/BF01993343.

Gunn, R. 1955. The statistical electrification of aerosols by ionic diffusion. *J. Colloid Sci* 10 (1):107–19. doi:10.1016/0095-8522(55)90081-7.

Hasenkopf, C. A., M. R. Beaver, M. G. Trainer, H. Langley Dewitt, M. A. Freedman, O. B. Toon, C. P. McKay, and M. A. Tolbert. 2010. Optical properties of Titan and early Earth haze laboratory analogs in the mid-visible. *Icarus* 207 (2):903–13. doi:10.1016/j.icarus.2009.12.015.

Haynes, W.M. (Ed.) 2015. Physical Constants of Inorganic Compounds. in *CRC Handbook of Chemistry and Physics*, Abingdon, Oxfordshire: CRC Press, Taylor & Francis Group. 4-43–101.

Haywood, J. M., and K. P. Shine. 1995. The effect of anthropogenic sulfate and soot aerosol on the clear sky planetary radiation budget. *Geophys. Res. Lett.* 22 (5): 603–6. doi:10.1029/95GL00075.

Hoppel, W. A. 1978. Determination of the aerosol size distribution from the mobility distribution of the charged fraction of aerosols. *J. Aerosol Sci* 9 (1):41–54. doi:10.1016/0021-8502(78)90062-9.

Kahnert, M., and F. Kanngießer. 2020. Modelling optical properties of atmospheric black carbon aerosols. *J. Quant. Spectrosc. Radiat. Transf.* 244:106849. doi:10.1016/j.jqsrt.2020.106849.

Khalizov, A. F., H. Xue, L. Wang, J. Zheng, and R. Zhang. 2009. Enhanced light absorption and scattering by carbon soot aerosol internally mixed with sulfuric acid. *J. Phys. Chem. A* 113 (6):1066–74. doi:10.1021/jp807531n.

Lack, D. A., E. R. Lovejoy, T. Baynard, A. Pettersson, and A. R. Ravishankara. 2006. Aerosol Absorption measurement using photoacoustic spectroscopy: Sensitivity, calibration, and uncertainty developments. *Aerosol Sci. Technol* 40 (9):697–708. doi:10.1080/02786820600803917.

Lack, D. A., M. S. Richardson, D. Law, J. M. Langridge, C. D. Cappa, R. J. McLaughlin, and D. M. Murphy. 2012. Aircraft instrument for comprehensive characterization of aerosol optical properties, part 2: Black and brown carbon absorption and absorption enhancement measured with photo acoustic spectroscopy. *Aerosol Sci. Technol* 46 (5):555–68. doi:10.1080/02786826.2011.645955.

Lambe, A. T., C. D. Cappa, P. Massoli, T. B. Onasch, S. D. Forestieri, A. T. Martin, M. J. Cummings, D. R. Croasdale, W. H. Brune, D. R. Worsnop, et al. 2013. Relationship between oxidation level and optical properties of secondary organic aerosol. *Environ. Sci. Technol.* 47 (12):6349–57. doi:10.1021/es401043j.

Langridge, J. M., M. S. Richardson, D. A. Lack, C. A. Brock, and D. M. Murphy. 2013. Limitations of the photoacoustic technique for aerosol absorption measurement at high relative humidity. *Aerosol Sci. Technol* 47 (11):1163–73. doi:10.1080/02786826.2013.827324.

Lang-Yona, N., Y. Rudich, E. Segre, E. Dinar, and A. Abo-Riziq. 2009. Complex refractive indices of aerosols retrieved by continuous wave-cavity ring down aerosol spectrometer. *Anal. Chem.* 81 (5):1762–9. doi:10.1021/ac8017789.

Lee, A. K. Y., R. Zhao, R. Li, J. Liggio, S. M. Li, and J. P. D. Abbatt. 2013. Formation of light absorbing organo-nitrogen species from evaporation of droplets containing glyoxal and ammonium sulfate. *Environ. Sci. Technol.* 47 (22):12819–26. doi:10.1021/es402687w.

Lee, J. K., S. Banerjee, H. G. Nam, and R. N. Zare. 2015. Acceleration of reaction in charged microdroplets. *Quart. Rev. Biophys.* 48 (4):437–44. doi:10.1017/S0033583515000086.

Li, W., J. Sun, L. Xu, Z. Shi, N. Riemer, Y. Sun, P. Fu, J. Zhang, Y. Lin, X. Wang, et al. 2016. A conceptual framework for mixing structures in individual aerosol particles. *J. Geophys. Res.* 121 (22):13,784–,798.

Liu, Y., and P. H. Daum. 2008. Relationship of refractive index to mass density and self-consistency of mixing rules for multicomponent mixtures like ambient aerosols. *J. Aerosol Sci* 39 (11):974–86. doi:10.1016/j.jaerosci.2008.06.006.

Miles, R. E. H., S. Rudić, A. J. Orr-Ewing, and, and J. P. Reid. 2010. Influence of uncertainties in the diameter and Refractive Index of calibration polystyrene beads on the retrieval of aerosol optical properties using cavity ring down spectroscopy. *J. Phys. Chem. A* 114 (26):7077–84. doi:10.1021/jp103246t.

Nakayama, T., K. Sato, Y. Matsumi, T. Imamura, A. Yamazaki, and A. Uchiyama. 2013. Wavelength and NO*x* dependent complex refractive index of SOAs generated from the photooxidation of toluene. *Atmos. Chem. Phys.* 13 (2):531–45. doi:10.5194/acp-13-531-2013.

Peers, F., P. Francis, C. Fox, S. J. Abel, K. Szpek, M. I. Cotterell, N. W. Davies, J. M. Langridge, K. G. Meyer, S. E. Platnick, et al. 2019. Observation of absorbing aerosols above clouds over the south-east Atlantic Ocean from the geostationary satellite SEVIRI – Part 1: Method description and sensitivity. *Atmos. Chem. Phys.* 19 (14): 9595–611. doi:10.5194/acp-19-9595-2019.

Peers, F., P. Francis, S. J. Abel, P. A. Barrett, K. N. Bower, M. I. Cotterell, I. Crawford, N. W. Davies, C. Fox, S. Fox, et al. 2019. Observation of absorbing aerosols above clouds over the South-East Atlantic Ocean from the geostationary satellite SEVIRI - Part 2: Comparison with MODIS and aircraft measurements from the CLARIFY-2017 field campaign. *Atmos. Chem. Phys.* 19 (14): 9595–611. doi:10.5194/acp-2019-1176.

Radney, J. G., and C. D. Zangmeister. 2018. Comparing aerosol refractive indices retrieved from full distribution and size- and mass-selected measurements. *J. Quant. Spectrosc. Radiat. Transf* 220:52–66. doi:10.1016/j.jqsrt.2018.08.021.

Sedlacek, A., and J. Lee. 2007. Photothermal interferometric aerosol absorption spectrometry. *Aerosol Sci. Technol* 41 (12):1089–101. doi:10.1080/02786820701697812.

Seinfeld, J. H., and S. N. Pandis. 2006. *Atmospheric Chemistry and Physics*, 2nd ed. Hoboken, NJ: John Wiley and Sons, Inc.

Stolzenburg, M. 1988. *An ultrafine aerosol size distribution measuring system*. Minnesota: University of Minnesota.

Sumlin, B. J., A. Pandey, M. J. Walker, R. S. Pattison, B. J. Williams, and R. K. Chakrabarty. 2017. Atmospheric photooxidation diminishes light absorption by primary brown carbon aerosol from biomass burning. *Environ. Sci. Technol. Lett.* 4 (12):540–5. doi:10.1021/acs.estlett.7b00393.

Szpek, K., M. I. Cotterell, N. W. Davies, C. Fox, D. Tiddeman, A. Wilson, J. Bowles, R. King, J. Kent, R. Smout-Day, et al. 2020. EXSCALABAR – a new instrument for high accuracy measurement of aerosol absorption and extinction from research aircraft. *Atmos. Meas. Tech*. (in prep.).

Tang, I. N., A. C. Tridico, and K. H. Fung. 1997. Thermodynamic and optical properties of sea salt aerosols. *J. Geophys. Res.* 102 (D19):23269–75. doi:10.1029/97JD01806.

Tigges, L., A. Jain, and H. J. Schmid. 2015a. On the bipolar charge distribution used for mobility particle sizing: Theoretical considerations. *J. Aerosol Sci* 88:119–34. doi:10.1016/j.jaerosci.2015.05.010.

Tigges, L., A. Wiedensohler, K. Weinhold, J. Gandhi, and H. J. Schmid. 2015b. Bipolar charge distribution of a soft X-ray diffusion charger. *J. Aerosol Sci* 90:77–86. doi:10.1016/j.jaerosci.2015.07.002.

Toole, J. R., L. Renbaum-Wolff, and G. D. Smith. 2013. A calibration technique for improving refractive index retrieval from aerosol cavity ring-down spectroscopy. *Aerosol Sci. Technol* 47 (9):955–65. doi:10.1080/02786826.2013.805875.

Toon, O. B., J. B. Pollack, and B. N. Khare. 1976. The optical constants of several atmospheric aerosol species: Ammonium sulfate, aluminum oxide, and sodium chloride. *J. Geophys. Res.* 81 (33):5733–48. doi:10.1029/JC081i033p05733.

Trainic, M., A. Abo Riziq, A. Lavi, and Y. Rudich. 2012. Role of interfacial water in the heterogeneous uptake of glyoxal by mixed glycine and ammonium sulfate aerosols. *J. Phys. Chem. A* 116 (24):5948–57. doi:10.1021/jp2104837.

Washenfelder, R. A., J. M. Flores, C. A. Brock, S. S. Brown, and Y. Rudich. 2013. Broadband measurements of aerosol extinction in the ultraviolet spectral region. *Atmos. Meas. Tech.* 6 (4):861–77. doi:10.5194/amt-6-861-2013.

Wiedensohler, A. 1988. An approximation of the bipolar charge distribution for particles in the submicron size range. *J. Aerosol Sci* 19 (3):387–9. doi:10.1016/0021-8502(88)90278-9.

Wiedensohler, A., E. Lütkemeier, M. Feldpausch, and C. Helsper. 1986. Investigation of the bipolar charge distribution at various gas conditions. *J. Aerosol Sci* 17 (3): 413–6. doi:10.1016/0021-8502(86)90118-7.

Xue, H., A. F. Khalizov, L. Wang, J. Zheng, and R. Zhang. 2009. Effects of dicarboxylic acid coating on the optical properties of soot. *Phys. Chem. Chem. Phys.* 11 (36):7869. doi:10.1039/b904129j.

Zarzana, K. J., C. D. Cappa, and M. A. Tolbert. 2014. Sensitivity of Aerosol Refractive Index retrievals using optical spectroscopy. *Aerosol Sci. Technol* 48 (11): 1133–44. doi:10.1080/02786826.2014.963498.

Zarzana, K. J., D. O. De Haan, M. A. Freedman, C. A. Hasenkopf, and M. A. Tolbert. 2012. Optical properties of the products of α-dicarbonyl and amine reactions in simulated cloud droplets. *Environ. Sci. Technol.* 46 (9): 4845–51. doi:10.1021/es2040152.